

An Improved Iterative Neural Network for High-Quality Image-Domain Material Decomposition in Dual-Energy CT

Zhipeng Li, *Student Member, IEEE*, Yong Long, *Member, IEEE*, and Il Yong Chun, *Member, IEEE*

Abstract—Dual-energy computed tomography (DECT) has been widely used in many applications that need material decomposition. Image-domain methods directly decompose material images from high- and low-energy attenuation images, and thus, are susceptible to noise and artifacts on attenuation images. To obtain high-quality material images, various data-driven methods have been proposed. Iterative neural network (INN) methods combine regression NNs and model-based image reconstruction algorithm. INNs reduced the generalization error of (noniterative) deep regression NNs, and achieved high-quality reconstruction in diverse medical imaging applications. BCD-Net is a recent INN architecture that incorporates imaging refining NNs into the block coordinate descent (BCD) model-based image reconstruction algorithm. We propose a new INN architecture, distinct cross-material BCD-Net, for DECT material decomposition. The proposed INN architecture uses distinct cross-material convolutional neural network (CNN) in image refining modules, and uses image decomposition physics in image reconstruction modules. The distinct cross-material CNN refiners incorporate distinct encoding-decoding filters and cross-material model that captures correlations between different materials. We interpret the distinct cross-material CNN refiner with patch perspective. Numerical experiments with extended cardiac torso (XCAT) phantom and clinical data show that proposed distinct cross-material BCD-Net significantly improves the image quality over several image-domain material decomposition methods, including a conventional model-based image decomposition (MBID) method using an edge-preserving regularizer, a state-of-the-art MBID method using pre-learned material-wise sparsifying transforms, and a noniterative deep CNN denoiser.

Index Terms—Dual-energy CT, iterative neural network, image-domain decomposition, cross-material models.

I. INTRODUCTION

Dual-energy CT (DECT) has been increasingly used in many clinical and industrial applications, including kidney stone characterization [1], iodine quantification [2], [3], security inspection [4], [5], and nondestructive testing [6]. Compared to conventional single-energy X-ray CT, DECT provides two sets of attenuation measurements by using two different energy spectra. Because the linear attenuation coefficient is material and energy dependent, DECT can characterize different constituent materials in a mixture, known as material

decomposition [7]. Decomposed material images provide the material compositions of the imaged object that is not available in single-energy CT.

A. Background

Model-based image decomposition (MBID) methods incorporate material composition physics, statistical model of measurements, and some prior information of unknown material images. Existing MBID methods for DECT can be classified into direct (projection-to-image domain) [8], projection-domain [9], and image-domain [10] decompositions. Direct decomposition methods perform image decomposition and reconstruction simultaneously, and generate material images directly from collected high and low energy measurements. This type of methods can reduce the cross-talk and beam-hardening artifacts by using an accurate forward model of the DECT system along with priors. However, direct decomposition algorithms need large computational costs, because at each iteration, they apply computationally expensive forward and backward projection operators. Projection-domain methods first decompose high and low energy sinograms into sinograms of materials, followed by an image reconstruction method such as filtered back projection (FBP) to obtain material images. Although above two types of methods improved the decomposition accuracy compared to image-domain methods, they usually require accurate system calibrations that use nonlinear models [11], [12]. In addition, those require sinograms or pre-log measurements that are in general not readily available from commercial CT scanners. Image-domain methods do not require projection operators and decompose readily available reconstructed high and low energy attenuation images into material images, and are more computationally efficient than direct and projection-domain decomposition methods. However, image-domain methods lack complete DECT imaging model. This may increase noise and artifacts in decomposed material images.

To improve image-domain DECT material decomposition, incorporating appropriate prior knowledge or regularizer into decomposition algorithms is critical. Many MBID methods have been proposed from this perspective. Niu *et al.* [10] proposed an iterative decomposition method that incorporates the noise variance of two attenuation images into the least-squares data-fit term. This better suppressed noise and artifacts on decomposed material images than a simple direct matrix inversion method. [13] proposed an MBID method that

This work was supported by NSFC (61501292). Yong Long and Il Yong Chun are corresponding authors.

Z. Li and Y. Long are with the University of Michigan - Shanghai Jiao Tong University Joint Institute, Shanghai Jiao Tong University, Shanghai 200240 China (email: zhipengli@sjtu.edu.cn, yong.long@sjtu.edu.cn).

Il Yong Chun is with the Department of Electrical Engineering, University of Hawai'i at Mānoa, Honolulu, HI 96801 USA (iyochun@hawaii.edu).

This paper has supplementary material. The prefix “S” indicates the numbers in section, equation, and figure in the supplementary material.

uses the weighted least-squares data-fit model [10] and an edge-preserving (EP) hyperbolic regularizer—called DECT-EP. Recently, there has been growing interest in data-driven methods such as MBID using pre-learned prior operators. Examples include learned synthesis operator/dictionary [14], [15] and analysis operator/transform [16], [17]. Dictionary learning has been applied to image-domain DECT material decomposition [15] and improved image decomposition compared to non-adaptive MBID methods. We proposed a data-driven method DECT-ST [17] that uses two pre-learned sparsifying transforms (ST) in a prior model to better sparsify the two different materials, and improved the image decomposition accuracy. We also proposed a clustering based cross-material method [18] that assumes correlations between different materials, and followed by a generalized mixed material method [19] that considers both individual properties (e.g., different materials have different densities and structures) and correlations of different material images.

In the past few years, deep regression neural network (NN) methods have been gaining popularity in medical imaging applications, for example, CT image denoising [20], [21]. Several deep convolutional NN (DCNN) methods have also been proposed for image-domain DECT material decomposition. [22] proposed a cascaded DCNN method to obtain material images from single energy attenuation image. The first DCNN roughly maps a single attenuation image to a material image, followed by the other DCNN maps the material image to a high-quality material image. [23] proposed a DCNN method with two input and output channels that directly maps from two high- and low-energy attenuation images to two material images. Different from the first DCNN in [22] that obtains two material images individually, butterfly network [24] uses additional CNNs between two attenuation images to perform information exchange. [25] investigated the conventional U-Net architecture for image-domain multi-material decomposition. However, the aforementioned methods have the high NN complexity that can increase the overfitting risk particularly when limited training samples are available.

An alternative approach is a so-called iterative NN (INN), which has been successfully applied to diverse imaging problems [26]–[32]. This approach incorporates iteration-wise image refining NNs into block-wise model-based image reconstruction algorithm. INN improved generalization capability compared to noniterative deep NN by balancing imaging physics and prior information estimated via refining CNNs, particularly when training samples are limited [28], [29]. BCD-Net [26], [30] is a state-of-the-art INN architecture that generalizes a block coordinate descent (BCD) algorithm using learned convolutional regularizers [14], [16], [33]. BCD-Net successfully applied to several medical applications such as low-dose CT [28] and low-count PET [29]. The initial version of this work was presented in a conference [34], where we used an MBID cost function for the model-based image reconstruction module of BCD-Net, and demonstrated that BCD-Net significantly improved image quality over DECT-EP and DECT-ST. We refer to this method as identical individual-material BCD-Net, since it uses the CNN refiner that has identical encoding-decoding architecture, i.e., each filter in

decoder is a rotated version of that in encoder, individually for two different materials (e.g., water and bone).

B. Contributions

To improve material decomposition performance in DECT, this paper proposes a new BCD-Net method that uses distinct cross-material CNN refiners. We refer to this method as *distinct cross-material BCD-Net*, because its image refiners use distinct encoding-decoding architecture, i.e., each filter in decoding convolution is distinct from that in encoding convolution, and cross-material model that captures correlations between different material images. We interpret the proposed distinct cross-material CNN architecture with the patch-based perspective. The patch-based interpretation reveals that the proposed CNN architecture has the cross-material property, and specializes to three variants, identical cross-material, distinct individual-material, and identical individual-material [34] CNN refiners. The quantitative and qualitative results with XCAT phantom and clinical data show that the proposed distinct cross-material BCD-Net architecture significantly improves the decomposition quality compared to its three simpler variants, and following recent image-domain decomposition methods: a state-of-the-art noniterative DCNN denoiser, a state-of-the-art MBID method, DECT-ST [17], that uses a learned regularizer in an unsupervised way, and the conventional MBID method, DECT-EP [13].

C. Organization

The rest of this paper is organized as follows. Section II proposes and describes the proposed distinct cross-material BCD-Net architecture for DECT image-domain MBID, and reformulates and interprets the distinct cross-material refining CNN architecture using the patch perspective. Section III provides training algorithms for different BCD-Net architectures. Section IV reports results and comparisons to state-of-the-art and conventional methods with XCAT phantom and clinical data. Finally, we make conclusions of this paper, and describe future work in Section V.

II. PROPOSED BCD-NET ARCHITECTURE

This section proposes the distinct cross-material BCD-Net architecture, interprets its CNN refiners, and discusses its three variations.

A. The Distinct Cross-material BCD-Net Architecture for DECT Material Decomposition

Each iteration of BCD-Net for DECT material decomposition consists of an MBID module and an image refining module. The MBID cost function uses a weighted least-squares (WLS) data-fit term that models the material composition physics and noise statistics in the measurements, and a regularizer (or a prior term) that uses refined material images from an iteration-wise image refining module. Each image refining module of distinct cross-material BCD-Net has a single-hidden layer CNN architecture that consists of encoding convolution, nonlinear thresholding, and decoding

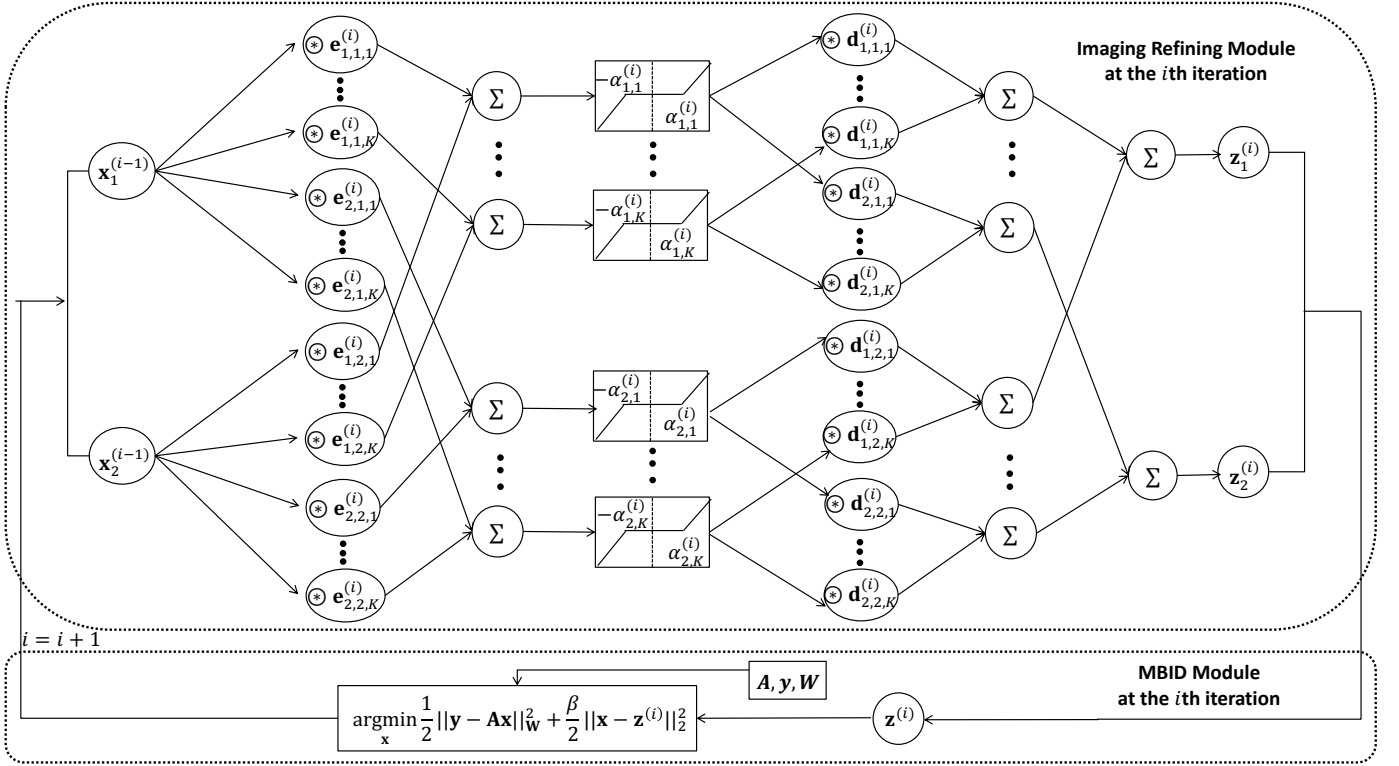


Fig. 1: Architecture of distinct cross-material BCD-Net at i th iteration, for $i = 1, \dots, I$.

convolution. We encode/decode each feature at a hidden layer by two groups of encoding/decoding filters. One is used to capture a feature of each material image individually, and the other is used to capture correlations between different material images. Different from DCNN denoiser that does not consider decomposition physics, the proposed BCD-Net architecture uses MBID module that is expected to be useful to reduce overfitting risks of CNN denoisers.

1) *Image Refining Module*: The i th image refining module of BCD-Net takes $\{\mathbf{x}_m^{(i-1)} \in \mathbb{R}^N : m = 1, 2\}$, decomposed material images at the $(i-1)$ th iteration, and outputs refined material images $\{\mathbf{z}_m^{(i)} \in \mathbb{R}^N : m = 1, 2\}$, for $i = 1, \dots, I$, where N is the number of pixels of each material image, and I is the number of BCD-Net iterations. Here, $\{\mathbf{x}_1, \mathbf{z}_1\}$, and $\{\mathbf{x}_2, \mathbf{z}_2\}$ denote water and bone images, respectively. We use the following single hidden-layer CNN architecture for each image refining module:

$$\mathcal{R}_{\Theta^{(i)}}(\mathbf{x}_1^{(i-1)}, \mathbf{x}_2^{(i-1)}) = \begin{bmatrix} \sum_{k=1}^K \sum_{n=1}^2 \mathbf{d}_{1,n,k}^{(i)} \otimes \mathcal{T}_{\exp(\alpha_{n,k}^{(i)})} \left(\sum_{m=1}^2 \mathbf{e}_{n,m,k}^{(i)} \otimes \mathbf{x}_m^{(i-1)} \right) \\ \sum_{k=1}^K \sum_{n=1}^2 \mathbf{d}_{2,n,k}^{(i)} \otimes \mathcal{T}_{\exp(\alpha_{n,k}^{(i)})} \left(\sum_{m=1}^2 \mathbf{e}_{n,m,k}^{(i)} \otimes \mathbf{x}_m^{(i-1)} \right) \end{bmatrix}, \quad (1)$$

where $\Theta^{(i)}$ denotes a set of parameters of image refining module at the i th iteration, i.e., $\Theta^{(i)} = \{\mathbf{d}_{m,n,k}^{(i)}, \mathbf{e}_{n,m,k}^{(i)}, \alpha_{n,k}^{(i)} : k = 1, \dots, K, m = 1, 2, n = 1, 2\}$, $\mathbf{d}_{m,n,k}^{(i)} \in \mathbb{R}^R$ and $\mathbf{e}_{n,m,k}^{(i)} \in \mathbb{R}^R$ are the k th decoding and encoding filters from the n th group of the m th material at the i th iteration, respectively, $\exp(\alpha_{m,k}^{(i)})$ is the k th thresholding value for the

m th material at the i th iteration, K is the number of filters in each encoding and decoding structure for each material, and R is the size of filters, $\forall m, n, k, i$. In (1), the element-wise soft thresholding operator $\mathcal{T}_{\mathbf{a}}(\mathbf{b}) : \mathbb{R}^N \rightarrow \mathbb{R}^N$ is defined by

$$(\mathcal{T}_{\mathbf{a}}(\mathbf{b}))_n := \begin{cases} b_n - a_n \cdot \text{sign}(b_n), & |b_n| > a_n \\ 0, & |b_n| \leq a_n, \end{cases} \quad (2)$$

for $n = 1, \dots, N$. We use the exponential function to thresholding parameters $\{\alpha_{n,k}\}$ to avoid thresholding values being negative [28], [30]. The first box in Fig. 1 shows the architecture of iteration-wise distinct cross-material CNNs. We will train distinct cross-material CNNs at each iteration to maximize the refinement performance.

The proposed CNN in (1) and Fig. 1 consists of an individual encoding-decoding architecture for each material image, and crossover architectures between different material images. When $n = m$, the filters in (1) form the individual encoding-decoding architecture that captures individual properties of the m th material, whereas when $n \neq m$, these comprise the crossover architecture that exchanges information between two material images. The crossover architecture is expected to be useful to remove noise and artifacts in material images; we will provide mathematical interpretation that supports the argument in Section II-C.

2) *MBID Module*: The i th MBID module of BCD-Net in the second box of Fig. 1 gives the decomposed material images, $\mathbf{x}^{(i)} = [(\mathbf{x}_1^{(i)})^\top, (\mathbf{x}_2^{(i)})^\top]^\top$, by reducing their deviations from attenuation maps $\mathbf{y} = [(\mathbf{y}_H)^\top, (\mathbf{y}_L)^\top]^\top$ and refined material images $\mathbf{z}^{(i)} = [(\mathbf{z}_1^{(i)})^\top, (\mathbf{z}_2^{(i)})^\top]^\top, \forall i$, where $\mathbf{y}_H \in \mathbb{R}^N$ and $\mathbf{y}_L \in \mathbb{R}^N$ are attenuation maps at high and low

energy, respectively. In particular, we measure the deviation of model-based decomposition $\mathbf{x}^{(i)}$ from attenuation maps \mathbf{y} , by using decomposition physics and noise statistics in \mathbf{y} . We formulate the MBID cost function by combining a WLS data-fit term and a regularizer using $\mathbf{z}^{(i)}$:

$$\begin{aligned} \mathbf{x}^{(i)} &= \underset{\mathbf{x} \in \mathbb{R}^{2N}}{\operatorname{argmin}} \frac{1}{2} \|\mathbf{y} - \mathbf{A}\mathbf{x}\|_{\mathbf{W}}^2 + G(\mathbf{x}), \\ G(\mathbf{x}) &= \beta \|\mathbf{x} - \mathbf{z}^{(i)}\|_2^2. \end{aligned} \quad (\text{P0})$$

The mass attenuation coefficient matrix $\mathbf{A} \in \mathbb{R}^{2N \times 2N}$ is a Kronecker product of \mathbf{A}_0 and identity matrix \mathbf{I}_N , i.e., $\mathbf{A} = \mathbf{A}_0 \otimes \mathbf{I}_N$, and the matrix $\mathbf{A}_0 \in \mathbb{R}^{2 \times 2}$ is defined as [17]:

$$\mathbf{A}_0 := \begin{bmatrix} \varphi_{1H} & \varphi_{2H} \\ \varphi_{1L} & \varphi_{2L} \end{bmatrix}, \quad (3)$$

in which φ_{mH} and φ_{mL} denote the mass attenuation coefficient of the m th material at high and low energy, respectively. In practice, these four values in matrix \mathbf{A} can be calibrated in advance by $\varphi_{mH} = \mu_{mH}/\rho_m$ and $\varphi_{mL} = \mu_{mL}/\rho_m$, where ρ_m denotes the density of the m th material (we use theoretical values 1 g/cm³ for water and 1.92 g/cm³ for bone in our experiment), and μ_{mH} and μ_{mL} denote the linear attenuation coefficient of the m th material at high and low energy, respectively. To obtain μ_{mH} and μ_{mL} , we manually select a uniform area in \mathbf{y}_H and \mathbf{y}_L (e.g., water region and bone region) respectively and compute the average pixel value in this area [10]. The weight matrix $\mathbf{W} \in \mathbb{R}^{2N \times 2N}$ is diagonal by assuming that high and low energy noise are uncorrelated [35]; it is represented as $\mathbf{W} = \mathbf{W}_0 \otimes \mathbf{I}_N$ by assuming the noise in each pixel of the attenuation images has equal variance [10]. Here, \mathbf{W}_0 is a 2×2 diagonal weight matrix with diagonal elements being the inverse of noise variance at high and low energies. The regularization parameter $\beta > 0$ controls the trade-off between noise and resolution in decompositions.

Based on the structures of matrices \mathbf{A} and \mathbf{W} above, we can separate the \mathbf{x} -update problem in (P0) into N subproblems. Then we obtain the following practical closed-form solution of \mathbf{x} at each pixel j :

$$\hat{\mathbf{x}}_j^{(i)} = (\mathbf{A}_0^\top \mathbf{W}_0 \mathbf{A}_0 + 2\beta \mathbf{I}_2)^{-1} (\mathbf{A}_0^\top \mathbf{W}_0 \mathbf{y}_j + 2\beta \mathbf{z}_j^{(i)}), \quad (4)$$

where $\hat{\mathbf{x}}_j^{(i)} = (\hat{x}_{1,j}, \hat{x}_{2,j})^\top$ denotes the water and bone density values at the j th pixel, $j = 1, \dots, N$. Due to small dimensions of matrices $\mathbf{A}_0^\top \mathbf{W}_0 \mathbf{A}_0$ and \mathbf{I}_2 , the matrix inversion in (4) is efficient; the cost to compute $\{\hat{\mathbf{x}}_j^{(i)} : \forall j\}$ scales as $O(N)$.

B. Variations of (1)

This section introduces three variants of the distinct cross-material CNN architecture in (1). We specialize (1) to have simpler components, and study three variants throughout the paper.

1) *Identical Cross-material BCD-Net*: This approach uses the following single-hidden layer CNN that has identical

encoding-decoding architectures and cross-material model:

$$\mathcal{R}_{\Theta^{(i)}}(\mathbf{x}_1^{(i-1)}, \mathbf{x}_2^{(i-1)}) = \left[\begin{array}{c} \sum_{k=1}^K \sum_{n=1}^2 \bar{\mathbf{e}}_{n,1,k}^{(i)} \otimes \mathcal{T}_{\exp(\alpha_{n,k}^{(i)})} \left(\sum_{m=1}^2 \mathbf{e}_{n,m,k}^{(i)} \otimes \mathbf{x}_m^{(i-1)} \right) \\ \sum_{k=1}^K \sum_{n=1}^2 \bar{\mathbf{e}}_{n,2,k}^{(i)} \otimes \mathcal{T}_{\exp(\alpha_{n,k}^{(i)})} \left(\sum_{m=1}^2 \mathbf{e}_{n,m,k}^{(i)} \otimes \mathbf{x}_m^{(i-1)} \right) \end{array} \right], \quad (5)$$

where $(\bar{\cdot})$ rotates a filter (e.g., it rotates 2D filters by 180°).

(1) specializes to (5) by setting $\mathbf{d}_{m,n,k}^{(i)}$ as $\bar{\mathbf{e}}_{n,m,k}^{(i)}$.

2) *Distinct Individual-material BCD-Net*: This approach uses following convolutional refiner that has distinct encoding-decoding architecture independently for two different material images:

$$\mathcal{R}_{\Theta_m^{(i)}}(\mathbf{x}_m^{(i-1)}) = \sum_{k=1}^K \mathbf{d}_{m,m,k}^{(i)} \otimes \mathcal{T}_{\exp(\alpha_{m,k}^{(i)})} \left(\mathbf{e}_{m,m,k}^{(i)} \otimes \mathbf{x}_m^{(i-1)} \right), \quad (6)$$

where $\Theta_m^{(i)}$ denotes a set of parameters for the m th material at the i th layer, i.e., $\Theta_m^{(i)} = \{\mathbf{e}_{m,m,k}^{(i)}, \mathbf{d}_{m,m,k}^{(i)}, \alpha_{m,k}^{(i)} : k = 1, \dots, K\}$. (1) specializes to (6) by setting $\mathbf{d}_{m,n,k}^{(i)} = \mathbf{e}_{n,m,k}^{(i)} = \mathbf{0}$ for $m \neq n$.

3) *Identical Individual-material BCD-Net*: This is a simpler convolutional autoencoder architecture proposed in our recent conference work [34], where

$$\mathcal{R}_{\Theta_m^{(i)}}(\mathbf{x}_m^{(i-1)}) = \sum_{k=1}^K \bar{\mathbf{e}}_{m,m,k}^{(i)} \otimes \mathcal{T}_{\exp(\alpha_{m,k}^{(i)})} \left(\mathbf{e}_{m,m,k}^{(i)} \otimes \mathbf{x}_m^{(i-1)} \right). \quad (7)$$

The specialized version (5) of (1) further specializes to (7) by setting $\mathbf{e}_{n,m,k}^{(i)} = \mathbf{0}$ for $m \neq n$.

C. Interpretations for Distinct Cross-Material CNN Refiner

This section interprets the district cross-material CNN (1) with patch perspective. We rewrite (1) with the patch perspective as follows (we omit the iteration superscript indices (i) for simplicity):

$$\mathcal{R}_{\Theta}(\mathbf{x}) \text{ in (1)} = \frac{1}{R} \sum_{j=1}^N \bar{\mathbf{P}}_j^\top \mathbf{D} \mathcal{T}_{\exp(\alpha)} (\mathbf{E} \bar{\mathbf{P}}_j \mathbf{x}), \quad (8)$$

where, $\bar{\mathbf{P}}_j = \mathbf{P}_j \oplus \mathbf{P}_j$, $\mathbf{P}_j \in \mathbb{R}^{R \times N}$ is the patch extraction operator for the j th pixel, $j = 1, \dots, N$, \oplus denotes the matrix direct sum, $\mathbf{D} \in \mathbb{R}^{2R \times 2K}$ and $\mathbf{E} \in \mathbb{R}^{2K \times 2R}$ are encoding and decoding filter matrices defined by:

$$\mathbf{D} := \begin{bmatrix} \mathbf{D}_{1,1} & \mathbf{D}_{1,2} \\ \mathbf{D}_{2,1} & \mathbf{D}_{2,2} \end{bmatrix} \text{ and } \mathbf{E} := \begin{bmatrix} \mathbf{E}_{1,1} & \mathbf{E}_{1,2} \\ \mathbf{E}_{2,1} & \mathbf{E}_{2,2} \end{bmatrix}, \quad (9)$$

$\mathbf{D}_{m,n}$ and $\mathbf{E}_{n,m}$ are formed by grouping filters $\{\mathbf{d}_{m,n,k}\}$ and $\{\mathbf{e}_{n,m,k}\}$, respectively, i.e.,

$$\begin{aligned} \mathbf{D}_{m,n} &:= [\mathbf{d}_{m,n,1}, \mathbf{d}_{m,n,2}, \dots, \mathbf{d}_{m,n,K}], \\ \mathbf{E}_{n,m} &:= [\mathbf{e}_{n,m,1}, \mathbf{e}_{n,m,2}, \dots, \mathbf{e}_{n,m,K}]^\top, \quad m, n = 1, 2, \end{aligned}$$

and $\alpha = [\alpha_{1,1}, \dots, \alpha_{1,K}, \alpha_{2,1}, \dots, \alpha_{2,K}]^\top \in \mathbb{R}^{2K}$ is a vector containing $2K$ thresholding parameters. We derived (8) using

the convolution to patch reformulation technique [30, S.8]; see Proposition S.1 for more details.

Both of encoding and decoding filter matrices, \mathbf{E} and \mathbf{D} , are composed of four smaller block matrices. Distinct individual-material CNN refiner uses only diagonal block matrices $\mathbf{E}_{1,1}$, $\mathbf{D}_{1,1}$ and $\mathbf{E}_{2,2}$, $\mathbf{D}_{2,2}$ as encoding and decoding filters for water and bone images, respectively, whereas distinct cross-material CNN refiner additionally uses off-diagonal block matrices $\mathbf{E}_{1,2}$, $\mathbf{D}_{1,2}$ and $\mathbf{E}_{2,1}$, $\mathbf{D}_{2,1}$ to exploit correlations between two material images. The number of trainable parameters are $2K(R+1)$, $2K(2R+1)$, $2K(2R+1)$, and $2K(4R+1)$ for identical individual-material, identical cross-material, distinct individual-material, and distinct cross-material CNN refiners, respectively. The crossover architecture captured via $\mathbf{E}_{1,2}$, $\mathbf{D}_{1,2}$ and $\mathbf{E}_{2,1}$, $\mathbf{D}_{2,1}$ will model shared structures between water and bone images at the same spatial locations. When trained with some image denoising loss, the crossover architecture with thresholding operator (2) is expected to better refine material images by exchanging shared noisy features between them, compared to the individual encoding-decoding case.

III. TRAINING BCD-NETS

This section describes training of distinct cross-material, identical cross-material, and distinct individual-material BCD-Nets.

A. Training Distinct Cross-Material BCD-Net

The training process at the i th iteration requires L input-output image pairs. Input labels are decomposed material images via MBID module, $\{\mathbf{x}_{l,m}^{(i-1)} : l = 1, \dots, L\}$, and output labels are high-quality reference material images, $\{\mathbf{x}_{l,m} : l = 1, \dots, L\}$. We use the patch-based training loss of $(1/L) \sum_{l=1}^L \|\mathbf{x}_l - \mathcal{R}_{\Theta}(\mathbf{x}_l^{(i-1)})\|_2^2$, where we derived their bound relation in Proposition S.2 using the convolution to patch loss reformulation techniques in [30, S.8]. Patch-based training first extracts reference and noisy material patches from $\{\mathbf{x}_{l,m} : l = 1, \dots, L\}$ and $\{\mathbf{x}_{l,m}^{(i-1)} : l = 1, \dots, L\}$ and constructs reference and noisy material data matrices $\tilde{\mathbf{X}}_m \in \mathbb{R}^{R \times P}$ and $\tilde{\mathbf{X}}_m^{(i-1)} \in \mathbb{R}^{R \times P}$, respectively, where $P = LN$. Then we construct paired multi-material data matrices $\tilde{\mathbf{X}} \in \mathbb{R}^{2R \times P}$ and $\tilde{\mathbf{X}}^{(i-1)} \in \mathbb{R}^{2R \times P}$, where each column is formed by stacking vectorized 2D patches extracted from the same spatial location in different material images. i.e., $\tilde{\mathbf{X}} = [\tilde{\mathbf{X}}_1^T, \tilde{\mathbf{X}}_2^T]^T$ and $\tilde{\mathbf{X}}^{(i-1)} = [(\tilde{\mathbf{X}}_1^{(i-1)})^T, (\tilde{\mathbf{X}}_2^{(i-1)})^T]^T$.

The training loss of distinct cross-material BCD-Net at the i th iteration is

$$\mathcal{L}(\mathbf{D}, \mathbf{E}, \alpha) := \frac{1}{P} \|\tilde{\mathbf{X}} - \mathbf{D} \mathcal{T}_{\exp(\alpha)}(\mathbf{E} \tilde{\mathbf{X}}^{(i-1)})\|_F^2, \quad (\text{P1})$$

where $\|\cdot\|_F$ denotes the Frobenius norm of a matrix. The subgradients of $\mathcal{L}(\mathbf{D}, \mathbf{E}, \alpha)$ with respect to \mathbf{D} , \mathbf{E} , and α for each mini-batch selection are as follows:

$$\frac{\partial \mathcal{L}(\mathbf{D}, \mathbf{E}, \alpha)}{\partial \mathbf{D}} = -\frac{2}{B} (\mathbf{X} - \mathbf{D} \mathbf{Z}^{(i-1)}) \mathbf{Z}^{(i-1)T} \quad (10)$$

$$\frac{\partial \mathcal{L}(\mathbf{D}, \mathbf{E}, \alpha)}{\partial \mathbf{E}} = -\frac{2}{B} \mathbf{D}^T (\mathbf{X} - \mathbf{D} \mathbf{Z}^{(i-1)}) \odot \mathbb{1}_{|\mathbf{E} \mathbf{X}^{(i-1)}| > \exp(\alpha \mathbf{1}')} \cdot \mathbf{X}^{(i-1)T} \quad (11)$$

Algorithm 1 Training Distinct Cross-material BCD-Net

Require: $\{\mathbf{x}_{l,m}, \mathbf{x}_{l,m}^{(0)}, \mathbf{y}_l, \mathbf{A}_l, \mathbf{W}_l : l = 1, \dots, L, m = 1, 2\}, \beta$

for $i = 1, 2, \dots, I$ **do**

 Train $\Theta^{(i)}$ via (P1) using $\{\mathbf{x}_{l,m}, \mathbf{x}_{l,m}^{(i-1)} : \forall l, m\}$

for $l = 1, \dots, L$ **do**

Refining: $(\mathbf{z}_{l,1}^{(i)}, \mathbf{z}_{l,2}^{(i)}) = \mathcal{R}_{\Theta^{(i)}}(\mathbf{x}_{l,1}^{(i-1)}, \mathbf{x}_{l,2}^{(i-1)})$

MBID: Obtain $\{\mathbf{x}_{l,m}^{(i)} : \forall l, m\}$ by solving (P0) with (4).

end for

end for

$$\frac{\partial \mathcal{L}(\mathbf{D}, \mathbf{E}, \alpha)}{\partial \alpha} = \frac{2}{B} \left\{ \mathbf{D}^T (\mathbf{X} - \mathbf{D} \mathbf{Z}^{(i-1)}) \odot \exp(\alpha \mathbf{1}') \odot \text{sign}(\mathbf{Z}^{(i-1)}) \right\} \mathbf{1}, \quad (12)$$

where $\mathbf{X}, \mathbf{X}^{(i-1)} \in \mathbb{R}^{2R \times B}$ are mini-batch in which columns are randomly selected from $\tilde{\mathbf{X}}$ and $\tilde{\mathbf{X}}^{(i-1)}$, respectively, $\mathbf{Z}^{(i-1)} = \mathcal{T}_{\exp(\alpha \mathbf{1}')}(\mathbf{E} \mathbf{X}^{(i-1)})$, and B is the mini-batch size. Here, $\mathbf{1} \in \mathbb{R}^{B \times 1}$ denotes a column vector of ones, $\mathbb{1}_{(\cdot)}$ is indicator function (value 0 when condition is violated and 1 otherwise), and \odot is the element-wise multiplication. The derivation details of (10)–(12) are in Section S.I. Once we obtain the learned filters and thresholding values, we apply them to refine material images. These refined images are then fed into the MBID module. Algorithm 1 shows the training process of distinct cross-material BCD-Net.

B. Training Identical Cross-Material BCD-Net

The training loss for identical cross-material BCD-Net at the i th iteration is

$$\mathcal{L}(\mathbf{E}, \alpha) := \frac{1}{P} \|\tilde{\mathbf{X}} - \mathbf{E}^T \mathcal{T}_{\exp(\alpha)}(\mathbf{E} \tilde{\mathbf{X}}^{(i-1)})\|_F^2.$$

The subgradient of $\mathcal{L}(\mathbf{E}, \alpha)$ with respect to \mathbf{E} and α for each mini-batch selection are obtained as follows:

$$\begin{aligned} \frac{\partial \mathcal{L}(\mathbf{E}, \alpha)}{\partial \mathbf{E}} &= -\frac{2}{B} (\mathbf{E} (\mathbf{X} - \mathbf{E}^T \mathbf{Z}^{(i-1)}) \odot \mathbb{1}_{|\mathbf{E} \mathbf{X}^{(i-1)}| > \exp(\alpha \mathbf{1}')} \mathbf{X}^{(i-1)T} - \frac{2}{B} \mathbf{Z}^{(i-1)} (\mathbf{X} - \mathbf{E}^T \mathbf{Z}^{(i-1)})^T \\ \frac{\partial \mathcal{L}(\mathbf{E}, \alpha)}{\partial \alpha} &= \frac{2}{B} \left\{ \mathbf{E} (\mathbf{X} - \mathbf{E}^T \mathbf{Z}^{(i-1)}) \odot \exp(\alpha \mathbf{1}') \odot \text{sign}(\mathbf{Z}^{(i-1)}) \right\} \mathbf{1} \end{aligned}$$

where $\mathbf{Z}^{(i-1)} = \mathcal{T}_{\exp(\alpha \mathbf{1}')}(\mathbf{E} \mathbf{X}^{(i-1)})$.

C. Training Individual-Material BCD-Nets

Distinct individual-material BCD-Net only involves submatrices $\mathbf{E}_{1,1}^{(i)}$, $\mathbf{D}_{1,1}^{(i)}$ and $\mathbf{E}_{2,2}^{(i)}$, $\mathbf{D}_{2,2}^{(i)}$, i.e., $\mathbf{E}_{1,2}^{(i)} = \mathbf{E}_{2,1}^{(i)} = \mathbf{D}_{2,1}^{(i)} = \mathbf{0}$ in (P1), and we train material-wise refining CNNs using image pair $(\tilde{\mathbf{X}}_m, \tilde{\mathbf{X}}_m^{(i-1)})$, $\forall m, i$; see details in Section S.II. See subgradients for training identical individual-material BCD-Net in [34].

IV. RESULTS AND DISCUSSIONS

This section describes experimental setup and reports comparison results with XCAT phantom [36] and clinical DECT head data. We compared the performances of the four proposed BCD-Net methods (distinct cross-material, distinct individual-material, identical cross-material, and identical individual-material [34] BCD-Nets), the conventional direct matrix inversion method, MBID methods using state-of-the-art data-driven and conventional non-data-driven regularizers, DECT-ST [17] and DECT-EP [13], and (noniterative) DCNN denoiser that uses a state-of-the-art depth and mode in the aforementioned datasets.

A. Methods for Comparisons

This section describes methods compared with the proposed BCD-Net methods. We will describe parameter details for proposed and compared methods in the next section.

1) *Direct Matrix Inversion* [10]: This conventional method solves (P0) with $G(\mathbf{x}) = 0$ by matrix inversion, i.e., $\mathbf{A}^{-1}\mathbf{y}$. We use direct matrix inversion results as initial material decomposition to DECT-EP and BCD-Nets, i.e., $\{\mathbf{x}^{(0)} = \mathbf{A}^{-1}\mathbf{y}\}$, and noisy input material images to DCNN denoiser.

2) *DECT-EP* [13]: This conventional method solves (P0) with a material-wise edge-preserving regularizer that is defined as $G_{EP}(\mathbf{x}) = \sum_{m=1}^2 \beta_m G_m(\mathbf{x}_m)$, where the m th material regularizer is $G_m(\mathbf{x}_m) = \sum_{j=1}^N \sum_{k \in S} \psi_m(x_{m,j} - x_{m,k})$, and S is a list of indices that correspond to neighboring pixels of a pixel $x_{m,j}$ with $|S| = R_{EP}$, $\forall m, j$. Here the potential function is $\psi_m(t) \triangleq \frac{\delta_m^2}{3} (\sqrt{1 + 3(t/\delta_m)^2} - 1)$ with the m th material EP parameter, δ_m . We chose β_m and δ_m for different materials separately to achieve the desired boundary sharpness and strength of smoothness.

3) *DECT-ST* [17]: This data-driven method solves (P0) with a state-of-the-art regularizer that uses two square material-wise sparsifying transforms trained in an unsupervised way, e.g., [16], [33]. The regularizer $R_{ST}(\mathbf{x})$ is defined as

$$G_{ST}(\mathbf{x}) \triangleq \min_{\{\mathbf{z}_{m,j}\}} \sum_{m=1}^2 \sum_{j=1}^N \beta_m \left\{ \|\Omega_m \mathbf{P}_{m,j} \mathbf{x} - \mathbf{z}_{m,j}\|_2^2 + \gamma_m^2 \|\mathbf{z}_{m,j}\|_0 \right\},$$

where $\Omega_1 \in \mathbb{R}^{R_{ST} \times R_{ST}}$ and $\Omega_2 \in \mathbb{R}^{R_{ST} \times R_{ST}}$ are pre-learned transforms for water and bone, respectively, $\mathbf{P}_{m,j} \mathbf{x}$ and $\mathbf{z}_{m,j}$ denote the j th patch of the m th material image and corresponding sparse vector, respectively, and R_{ST} is the number of pixels in each patch.

4) *DCNN Denoiser*: The (noniterative) image denoising DCNN method uses two input and output channels; specifically, it takes noisy water and bone images and provides denoised water and bone images. The architecture corresponds to the second CNN architecture of the cascaded DCNN [22].

B. Experimental Setup

1) *Imaging setup for XCAT phantom experiments*: We used 1024×1024 material images with pixel size $0.49 \times 0.49 \text{ mm}^2$ of the XCAT phantom in our imaging simulation. We generated noisy (Poisson noise) sinograms of size 888 (radial samples) $\times 984$ (angular views) using GE LightSpeed X-ray CT

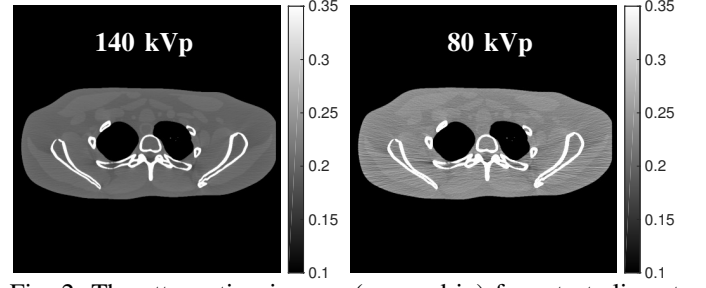


Fig. 2: The attenuation images (zoomed-in) for a test slice at high and low energies, respectively.

fan-beam system geometry corresponding to a poly-energetic source at 80 kVp and 140 kVp with 1.86×10^5 and 1×10^6 incident photons per ray, respectively. We used FBP method to reconstruct 2D high- and low-energy attenuation images of size 512×512 with a coarser pixel size $0.98 \times 0.98 \text{ mm}^2$ to avoid an inverse crime. Fig. 2 displays the attenuation images for a test slice.

2) *Data construction*: We separated each 1024×1024 slice of the original XCAT phantom into water and bone images according to the table of linear attenuation coefficients for organs provided for the XCAT phantom. We manually grouped fat, muscle, water, and blood into the water density images, and rib bone and spine bone into bone density images. We then downsampled these material density images to size 512×512 by linear averaging to generate ground truths of the decomposed material images. Fig. 3 shows ground truths of water and bone density images for a test slice. We chose 13 slices from the XCAT phantom that has 154 slices, among which $L = 10$ slices were used for training, and remaining 3 slices were used for testing. Testing phantom images are sufficiently different from training phantom images; specifically, they are at a minimum $\approx 1.5 \text{ cm}$ away, i.e., 25 slices. For DCNN, we used $L = 20$ slices of XCAT phantom that includes the 10 slices chosen for BCD-Nets training. In general, DCNNs need many training samples, so we used more image pairs to train DCNN compared to BCD-Nets.

In addition, using clinical data, we evaluated the proposed methods and compared them to the methods in Section IV-A. The patient head data was obtained by Siemens SOMATOM Definition flash CT scanner using dual-energy CT imaging protocols. The protocols of this head data acquisition are listed in Table I. For dual-energy data acquisition, the dual-energy source were set at 140 kVp and 80 kVp. Fig. 4 shows attenuation images of head data. FBP method was used to reconstruct these attenuation images.

3) *DECT-EP*: We first obtained the low-quality material images from high- and low-energy attenuation images using direct matrix inversion method, and used these results to initialize DECT-EP method. We used the 8-neighborhood system, $R_{EP} = 8$. To ensure convergence, we ran DECT-EP with 500 iterations. We tuned the parameters $\{\beta_m, \delta_m : m = 1, 2\}$ to achieve the best image quality and decomposition accuracy. For XCAT phantom, we set them as $\{2^8, 0.01\}$ and $\{2^{8.5}, 0.02\}$ for water and bone, respectively; for patient head data, we set them as $\{2^{10.5}, 0.008\}$ and $\{2^{11}, 0.015\}$ for water and bone, respectively.

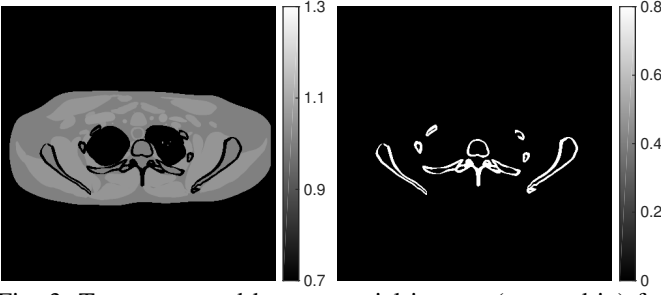


Fig. 3: True water and bone material images (zoomed-in) for a test slice.

TABLE I: Data acquisition parameters applied in head data acquisition.

Scanner	Head Data	
	High-energy	Low-energy
Peak Voltage(kVp)	140	80
X-ray Tube Current (mA)	364	648
Exposure Time (s)	0.285	
Current-exposure Time Product (mAs)	103.7	184.7
Noise STD (mm^{-1})	1.57×10^{-4}	3.61×10^{-4}
Helical Pitch	0.7	
Gantry Rotation Speed (circle/second)	0.28	

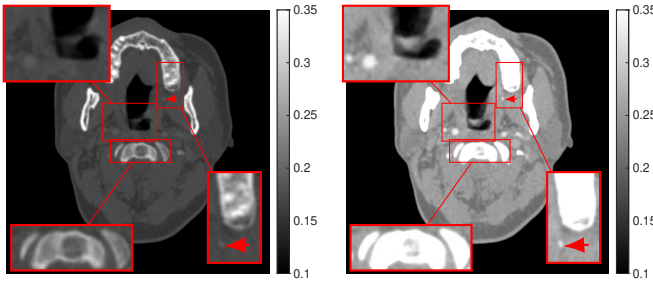


Fig. 4: Head CT images at 140 kVp (left) and 80 kVp (right). The display window is $[0.1 \ 0.35] \text{ cm}^{-1}$.

4) *DECT-ST*: We pre-learned two sparsifying transform matrices of size $R_{\text{ST}}^2 = 64^2$ with ten slices (same slices as used in training BCD-Nets) of true water and bone images of the XCAT phantom, using the suggested algorithm and parameter set (including number of iterations, regularization parameters, transform initialization, etc.) in [17]. We initialized DECT-ST using decomposed images obtained by DECT-EP method. We tuned the parameters $\{\beta_1, \beta_2, \gamma_1, \gamma_2\}$ to achieve the best image quality and decomposition accuracy: we set them as $\{50, 70, 0.03, 0.04\}$ for XCAT phantom, and $\{150, 200, 0.012, 0.024\}$ for patient head data.

5) *DCNN denoiser*: For the denoising DCNN architecture, we set the number of layers and number of features in hidden layers as 4 and 64, respectively. We did not use batch

normalization and bias because the pixel values of different training/testing images are of the same scale. We learned the DCNN denoiser \mathcal{R} with the *de facto* standard loss in image denoising, $\mathcal{L}(\mathcal{R}) = \frac{1}{L} \sum_{l=1}^L \|\mathbf{x}_l - \mathcal{R}(\mathbf{x}_l^{(0)})\|_2^2$, with Adam using 200 epochs and batch size 1. We observed with the clinical data that selected DCNN architecture gives better decomposed image quality, compared to its variants with 8 layers and/or the different mode that maps high and low energy attenuation images to two material images (this mode corresponds to [23]–[25]).

6) *BCD-Nets*: We trained four 100-iteration BCD-Nets, each with a different image refining CNN architecture in (1) and (5)–(7). We initialized all filters with values randomly generated from a Gaussian distribution with a zero mean and standard deviation of 0.1. For both distinct and identical cross-material BCD-Nets, we trained cross-material CNN refiners with about 1×10^6 paired stacked multi-material patches. At each iteration, we trained $8K = 512$ filters of size $R = 8 \times 8$ for distinct cross-material BCD-Net, and $4K = 256$ filters of size $R = 8 \times 8$ for identical cross-material BCD-Net. For both distinct and identical individual-material BCD-Nets, we trained convolutional refiners for each material with about 1×10^6 paired patches. At each iteration, we trained $2K = 128$ filters of size $R = 8 \times 8$ for each material of distinct individual-material BCD-Net, and $K = 64$ filters of size $R = 8 \times 8$ for each material of identical individual-material BCD-Net. We found in training that thresholding value initialization is important to ensure stable performances. For individual-material BCD-Nets, we set initial thresholding parameters before applying the exponential function as $\log(0.88)$ and $\log(0.8)$ for water and bone, respectively; for cross-material BCD-Nets, we set them as $\log(0.88)$. The regularization parameter β balances data-fit term and the prior estimate from image refining module. To achieve the best image quality and decomposition accuracy, we set β as 300, 1600, 1600, and 3200 for identical individual-material, distinct individual-material, identical cross-material, and distinct cross-material BCD-Nets, respectively (note that different BCD-Net architectures have different refining performance). We solved (P1) and its variations with Adam [37] using the default hyperparameters and tuned learning rate of 3×10^{-4} . We applied the learning rate schedule that decreases learning rates by a ratio of 90% every five epochs. We set batch size and number of epochs as $B = 10000$ and 50, respectively.

For patient head data, we used the learned filters and thresholding values with XCAT phantom. The attenuation maps of XCAT phantom and clinical head data were generated by different energy spectrum and dose, and the clinical head data is much more complex than the XCAT phantom (see Figs. 2 and 4). We thus set different regularization parameter β for the patient head data to achieve the best image quality; specifically, we set β as 1500, 3000, 2000, 6000 in testing identical individual-material, identical cross-material, distinct individual-material, and distinct cross-material BCD-Nets, respectively.

7) *Evaluation metric*: In the quantitative evaluations with the XCAT phantom, we computed root-mean-square error (RMSE) for decomposed material images within a region

TABLE II: RMSE of decomposed material density images obtained by different methods for three different test slices of XCAT phantom. The unit for RMSE is 10^{-3} g/cm^3 .

Methods	Test #1		Test #2		Test #3	
	water	bone	water	bone	water	bone
Direct matrix inversion	91.2	89.0	70.4	69.9	119.2	111.9
DECT-EP	60.0	68.5	59.5	63.3	69.9	75.9
DECT-ST	54.2	60.3	52.1	54.1	62.5	66.3
DCNN	21.9	24.3	19.8	20.8	24.9	30.2
Iden. indiv.-material BCD-Net	44.4	39.1	37.0	33.4	47.2	48.8
Iden. cross-material BCD-Net	30.5	34.7	29.7	31.9	42.5	45.3
Dist. indiv.-material BCD-Net	37.4	34.0	34.2	29.9	36.6	38.6
Dist. cross-material BCD-Net	23.0	25.3	20.2	23.2	22.2	27.6

of interest (ROI). We set the ROI as a circle region that includes all the phantom tissue. For a decomposed material density image \hat{x}_m , the RMSE in density (g/cm^3) is defined as $\sqrt{\sum_{j=1}^{N_{ROI}} (\hat{x}_{m,j} - x_{m,j}^*)^2 / N_{ROI}}$, where $x_{m,j}^*$ denotes the true density value of m th material at the j th pixel location, and N_{ROI} is the number of pixels in a ROI.

C. Decomposition Results with XCAT Phantom

Table II summarizes the RMSE values of material images decomposed by various methods for three different test slices. Cross-material BCD-Nets significantly decrease RMSE for material images compared to direct matrix inversion, DECT-EP, DECT-ST, and individual-material BCD-Nets. For all the test phantom samples, distinct cross-material BCD-Net achieves the lowest RMSE values among different BCD-Net architectures. Distinct cross-material BCD-Net and DCNN methods achieve comparable errors: distinct cross-material BCD-Net achieves an average $0.4 \times 10^{-3} \text{ g/cm}^3$ improvement for water images over DCNN, while DCNN achieves an average $0.2 \times 10^{-3} \text{ g/cm}^3$ improvement for bone images over distinct cross-material BCD-Net.

Fig. 5 shows the #3 material density images decomposed by direct matrix inversion, DECT-EP, DECT-ST, DCNN, and distinct cross-material BCD-Net. DECT-EP reduces severe noise and artifacts in direct matrix inversion decompositions. DECT-ST and DCNN improve the image quality visually compared to DECT-EP, but still retain obvious artifacts. Compared to DECT-ST and DCNN, distinct cross-material BCD-Net further removes the noise and artifacts while improving the sharpness of edges in soft tissue. These improvements are clearly noticeable in the zoom-ins of water images. We show the results of identical individual-material, identical cross-material, and distinct individual-material BCD-Nets in Fig. S.1. Another two test slices comparisons are included in Figs. S.2–S.3.

Compared to the other methods, the proposed distinct cross-material BCD-Net significantly suppresses noise and artifacts,

especially the areas at the boundaries of water and bone. Distinct cross-material BCD yet has limited performance in removing beam-hardening artifacts; the circles in left zoom-ins of Fig. 5 show beam-hardening artifacts on a bone region. Beam-hardening artifacts is an inherent problem of image-domain methods; it is challenging to completely remove them via image-domain MBID methods since they already exist in attenuation images.

D. Decomposition Results with Patient Data

Fig. 6 shows decomposed material density images by direct matrix inversion, DECT-EP, DECT-ST, DCNN, and distinct cross-material BCD-Net. DECT-EP reduces severe noise and artifacts in direct matrix inversion results, but it is difficult to distinguish edges in many soft tissue regions. DECT-ST and DCNN suppress noise and improve the edge in soft tissues compared to DECT-EP, but both still have poor contrast in many soft tissue regions. Distinct cross-material BCD-Net can better remove noise and artifacts, provides clearer image edges and structures, and recovers better details, compared to other methods. One clearly noticeable improvement is captured in the leftmost zoom-ins in water images, where distinct cross-material BCD-Net not only improves edge sharpness and contrast in soft tissue, but also suppresses bright artifacts. Inside red circle 1 in water images, distinct cross-material BCD-Net preserves a “dark spot” that exists in attenuation images in Fig. 4, whereas DECT-EP, DECT-ST and DCNN all missed it. The structure of the dark spot is an artery that contains diluted iodine solution caused by angiogram. The linear attenuation coefficient of iodine is much closer to bone than soft-tissue. During decomposition, most of the iodine is grouped into the bone image, while in the water image there are only some pixels with tiny values, thus it is a dark spot. Moreover, the marrow structures obtained by distinct cross-material BCD-Net have sharper edges (inside red circle 2) than the other four methods, and improvements can be also observed at the same spatial location in water images (inside red circle 3). Fig. S.5 additionally illustrates that distinct cross-material BCD-Net provides better decomposition quality over other three BCD-Nets.

Similar to XCAT phantom results, the DCNN denoiser gives less appealing material images of the clinical head data, compared to distinct cross-material BCD-Net. We conjecture that the following reasons may limit the DCNN denoising performance: lack of considering decomposition physics and/or limited training samples and diversity. The proposed distinct cross-material BCD-Net method resolves the issues by using MBID cost minimization and shallow-and-wide CNN refiner at each iteration. The clinical head data shows that distinct cross-material BCD-Net successfully reduces noise/artifacts and preserves subtle details that exist in attenuation images in Fig. 4.

E. Computational Complexity Comparisons

The computational cost of DECT-EP, DECT-ST, DCNN in Section IV-A4, and BCD-Nets scale as $O(R_{EP}N I_{EP})$, $O((R_{ST})^2 N I_{ST})$, $O(R_{CNN} K_{CNN} N ((C - 2) K_{CNN} + 4))$, and

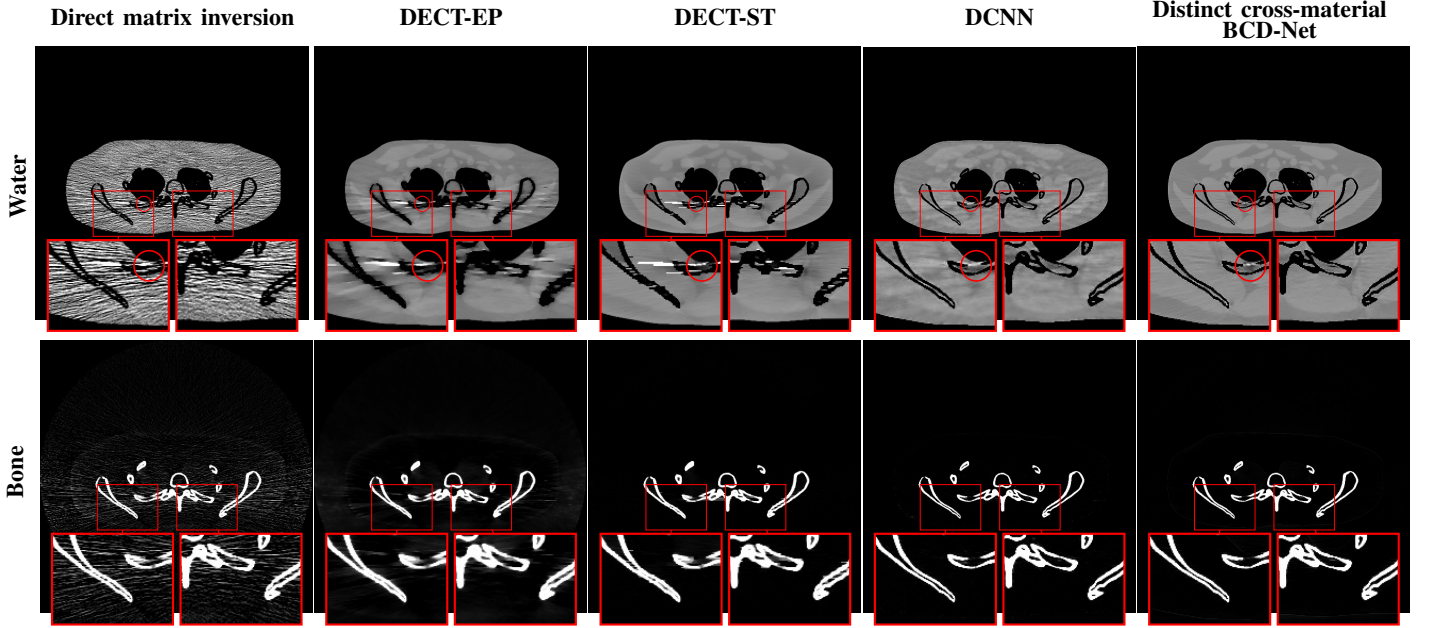


Fig. 5: Material decomposition results of a test slice. The top and bottom rows show the water and bone images with display windows $[0.7 \ 1.3] \text{ g/cm}^3$ and $[0 \ 0.8] \text{ g/cm}^3$, respectively.

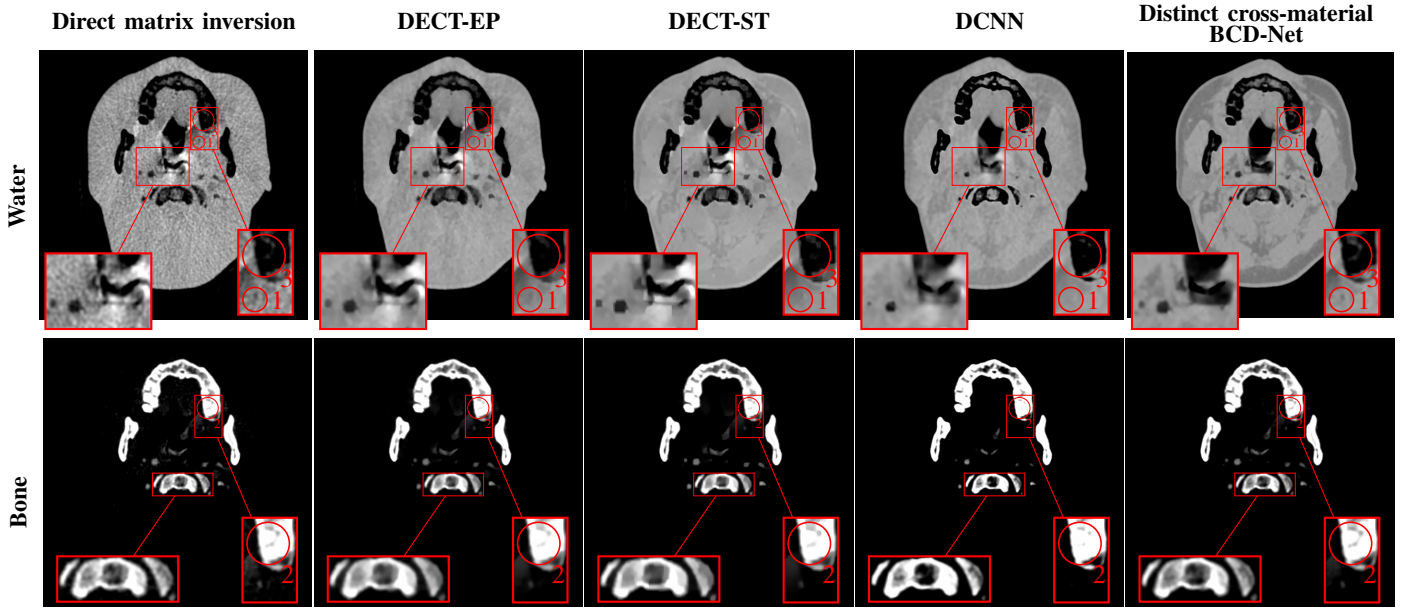


Fig. 6: Material decomposition results for clinical head data. The top and bottom rows represent water and bone images with display windows $[0.5 \ 1.3] \text{ g/cm}^3$ and $[0.05 \ 0.905] \text{ g/cm}^3$, respectively.

$O(RKNI)$, respectively, where I_{EP} and I_{ST} are the number of iterations for DECT-EP and DECT-ST, respectively, and R_{CNN} , K_{CNN} , and C are kernel size, the number of features, and the number of convolutional layers of DCNN denoiser, respectively. In all experiments, we used $R_{EP} = 8$ and $I_{EP} = 500$ for DECT-EP, $R_{ST} = 64$ and $I_{ST} = 1000$ for DECT-ST, $R_{CNN} = 3^2$, $K_{CNN} = 64$, and $C = 4$ for DCNN denoiser, and $R = K = 8^2$ and $I = 100$ for four BCD-Net methods. The big-O analysis reveals that the computational cost of 100-iteration BCD-Nets is larger than 500-iteration DECT-EP and the chosen DCNN denoiser, and 90% cheaper than that of 1000-iteration DECT-ST.

V. CONCLUSIONS

Image-domain decomposition methods are readily applicable to commercial DECT scanners, but susceptible to noise and artifacts on attenuation images. To improve MBID performance, it is important to incorporate accurate prior knowledge into sophisticatedly designed MBID. The proposed distinct cross-material BCD-Net architecture successfully achieves accurate MBID by providing accurate prior knowledge via its iteration-wise refiners that exploit correlations between different material images with distinct encoding-decoding filters. Our patch-based interpretation reveals the cross-material property. On both XCAT phantom and patient head data, distinct

cross-material BCD-Net reduces the artifacts at boundaries of materials and improves edge sharpness and contrast in soft tissue, compared to a conventional MBID method, DECT-EP, a state-of-the-art MBID method, DECT-ST, and a state-of-the-art noniterative DCNN denoiser.

The proposed INN architecture has room for further improvements. To further improve the MBID model, we plan to train the weight matrix \mathbf{W}_0 in (P0) in a supervised way with proper loss function designs, rather than statistically estimating it. By extending the patch-perspective interpretations, we will develop an “explainable” deeper refiner that might further improve the MBID performance of BCD-Net. To accommodate the non-trivial tuning process of β in (P0), we plan to learn it from training datasets.

VI. ACKNOWLEDGEMENT

The authors thank Dr. Tianye Niu, Georgia Institute of Technology, for providing clinical DECT images for our experiments.

REFERENCES

- [1] N. Hokamp, S. Lennartz, J. Salem, D. P. Santos, A. Heidenreich, D. Maintz, and S. Haneder. Dose independent characterization of renal stones by means of dual energy computed tomography and machine learning: an ex-vivo study. *European Radiology*, 30(3):1397–1404, 2020.
- [2] M. C. Jacobsen, E. N. Cressman, E. P. Tamm, D. L. Baluya, X. Duan, D. D. Cody, D. Schellingerhout, and R. R. Layman. Dual-energy CT: lower limits of iodine detection and quantification. *Radiology*, 292(2):414–419, 2019.
- [3] Y. Li, G. Shi, S. Wang, S. Wang, and R. Wu. Iodine quantification with dual-energy CT: phantom study and preliminary experience with VX2 residual tumour in rabbits after radiofrequency ablation. *British Journal of Radiology*, 86(1029):143–151, 2013.
- [4] Y. Liu, J. Cheng, Z. Chen, and Y. Xing. Feasibility study: Low-cost dual energy CT for security inspection. In *Proc. IEEE Nuc. Sci. Symp. Med. Im. Conf.*, pages 879–882, 2010.
- [5] L. Martin, A. Tuysuzoglu, W. C. Karl, and P. Ishwar. Learning-based object identification and segmentation using dual-energy CT images for security. *IEEE Trans. Im. Proc.*, 24(11):4069–4081, 2015.
- [6] Philip Engler and William D. Friedman. Review of dual-energy computed tomography techniques. *Materials Evaluation*, 48(5):623–629, 1990.
- [7] P. R. S. Mendonca, P. Lamb, and D. Sahani. A flexible method for multi-material decomposition of dual-energy CT images. *IEEE Trans. Med. Imag.*, 33(1):99–116, January 2014.
- [8] Y. Long and J. A. Fessler. Multi-material decomposition using statistical image reconstruction for spectral CT. *IEEE Trans. Med. Imag.*, 33(8):1614–1626, August 2014.
- [9] J. Noh, J. A. Fessler, and P. E. Kinahan. Statistical sinogram restoration in dual-energy CT for PET attenuation correction. *IEEE Trans. Med. Imag.*, 28(11):1688–1702, November 2009.
- [10] T. Niu, X. Dong, M. Petrongolo, and L. Zhu. Iterative image-domain decomposition for dual-energy CT. *Med. Phys.*, 41(4):041901, April 2014.
- [11] M. M. Goodsitt, E. G. Christodoulou, and S. C. Larson. Accuracies of the synthesized monochromatic CT numbers and effective atomic numbers obtained with a rapid kVp switching dual energy CT scanner. *Med. Phys.*, 38(4):2222–2232, April 2011.
- [12] M. Daniele, T.B. Daniel, M. Achille, and C. N. Rendon. State of the art: Dual-Energy CT of the abdomen. *Radiology*, 271(2):327–342, May 2014.
- [13] Y. Xue, R. Ruan, X. Hu, Y. Kuang, J. Wang, Y. Long, and T. Niu. Statistical image-domain multi-material decomposition for dual-energy CT. *Med. Phys.*, 44(3):886–901, 2017.
- [14] I. Y. Chun and J. A. Fessler. Convolutional dictionary learning: Acceleration and convergence. *IEEE Trans. Im. Proc.*, 27(4):1697–1712, Apr. 2018.
- [15] P. Chen F. Luo F. Liu Q. Wang Y. Zhu Y. Zhang J. Feng W. Wu, H. Yu and H. Yu. DLIMD: Dictionary learning based image-domain material decomposition for spectral CT. May 2019. Online: <https://arxiv.org/abs/1905.02567>.
- [16] I. Y. Chun and J. A. Fessler. Convolutional analysis operator learning: Acceleration and convergence. *IEEE Trans. Im. Proc.*, 29:2108–2122, 2020.
- [17] Z. Li, S. Ravishankar, Y. Long, and J. A. Fessler. Image-domain material decomposition using data-driven sparsity models for dual-energy CT. In *Proc. IEEE Intl. Symp. Biomed. Imag.*, pages 52–56, April 2018.
- [18] Z. Li, S. Ravishankar, and Y. Long. Image-domain multi-material decomposition using a union of cross-material models. In *Proc. Intl. Mtg. on Fully 3D Image Recon. in Rad. and Nuc. Med.*, pages 1107210–1–1107210–5, 2019.
- [19] Z. Li, S. Ravishankar, Y. Long, and J. A. Fessler. DECT-MULTRA: Dual-energy CT image decomposition with learned mixed material models and efficient clustering. *IEEE Trans. Med. Imag.*, 39(4):1223–1234, 2020.
- [20] D. Wu, K. Kim, G. Fakhri, and Q. Li. A cascaded convolutional neural network for X-ray low-dose CT image denoising. Aug. 2017. Online: <http://arxiv.org/abs/1705.04267>.
- [21] E. Froustey K. H. Jin, M. T. McCann and M. Unser. Deep convolutional neural network for inverse problems in imaging. *IEEE Trans. Im. Proc.*, 26(9):4509–4522, 2017.
- [22] Y. Liao, Y. Wang, S. Li, J. He, D. Zeng, Z. Bian, and J. Ma. Pseudo dual energy CT imaging using deep learning-based framework: basic material estimation. In *Proc. SPIE*, volume 10573, page 105734N, Mar. 2018.
- [23] Y. Xu, B. Yan, J. Zhang, J. Chen, L. Zeng, and L. Wang. Image decomposition algorithm for dual-energy computed tomography via fully convolutional network. *Comput. Math. Methods Med.*, Sep. 2018.
- [24] W. Zhang, H. Zhang, L. Wang, X. Wang, A. Cai, L. Li, T. Niu, and B. Yan. Image domain dual material decomposition for dual-energy CT using butterfly network. *Med. Phys.*, 46(5):2037–2051, May 2019.
- [25] D. P. Clark, M. Holbrook, and C. T. Badea. Multi-energy CT decomposition using convolutional neural networks. In *Medical Imaging 2018: Physics of Medical Imaging*, volume 10573, page 105731O, October 2018.
- [26] I. Y. Chun and J. A. Fessler. Deep BCD-Net using identical encoding-decoding CNN structures for iterative image recovery. In *Proc. IEEE Wkshp. on Image, Video, Multidim. Signal Proc.*, pages 1–5, 2018.
- [27] I. Y. Chun, H. Lim, Z. Huang, and J. A. Fessler. Fast and convergent iterative signal recovery using trained convolutional neural networks. In *Proc. Allerton Conf. on Commun., Control, and Comput.*, pages 155–159, Allerton, IL, Oct. 2018.
- [28] I. Y. Chun, X. Zheng, Y. Long, and J. A. Fessler. BCD-Net for low-dose CT reconstruction: Acceleration, convergence, and generalization. *Medical Image Computing and Computer-Assisted Intervention (MICCAI)*, pages 31–40, Oct. 2019.
- [29] H. Lim, I. Y. Chun, Y. K. Dewaraja, and J. A. Fessler. Improved low-count quantitative PET reconstruction with an iterative neural network. *IEEE Trans. Med. Imag.*, May 2020. DOI: 10.1109/TMI.2020.2998480.
- [30] I. Y. Chun, Z. Huang, H. Lim, and J. A. Fessler. Momentum-Net: Fast and convergent iterative neural network for inverse problems. early access in *IEEE Trans. Pattern Anal. Mach. Intell.*, Jul. 2020. DOI: 10.1109/TPAMI.2020.3012955.
- [31] S. Ye, Y. Long, and I. Y. Chun. Momentum-Net for low-dose CT image reconstruction. accepted to *Asilomar Conf. on Signals, Syst., and Comput.*, Aug. 2020. Online: <http://arxiv.org/abs/2002.12018>.
- [32] Y. Yang, J. Sun, H. Li, and Z. Xu. Deep ADMM-Net for compressive sensing MRI. In *Advances in Neural Information Processing Systems* 29, pages 10–18, December 2016.
- [33] I. Y. Chun, D. Hong, B. Adcock, and J. A. Fessler. Convolutional analysis operator learning: Dependence on training data. *IEEE Signal Proc. Letters*, 26(8):1137–1141, Jun. 2019. Online: <http://arxiv.org/abs/1902.08267>.
- [34] Z. Li, I. Y. Chun, and Y. Long. Image-domain material decomposition using an iterative neural network for dual-energy CT. In *Proc. IEEE Intl. Symp. Biomed. Imag.*, pages 651–655, April 2020.
- [35] R. Zhang, J. B. Thibault, C. A. Bouman, K. D. Sauer, and J. Hsieh. Model-based iterative reconstruction for dual-energy X-ray CT using a joint quadratic likelihood model. *IEEE Trans. Med. Imag.*, 33(1):117–134, January 2014.
- [36] W. P. Segars, M. Mahesh, T. J. Beck, E. C. Frey, and B. M. W. Tsui. Realistic CT simulation using the 4D XCAT phantom. *Med. Phys.*, 35(8):3800–3808, August 2008.
- [37] D. P. Kingma and J. L. Ba. Adam: A method for stochastic optimization. In *Proc. ICLR*, pages 1–15, May 2015.

An Improved Iterative Neural Network for High-Quality Image-Domain Material Decomposition in Dual-Energy CT – Supplementary Material

This supplement provides details for optimizing the training loss function in (P1), training of individual-material BCD-Nets, relation between convolution-perspective and patch-based trainings for distinct cross-material CNN refiner in (1), and additional experimental results to accompany our main manuscript [1]. We use the prefix “S” for the numbers in section, proposition, equation, and figure in the supplementary material.

S.I. OPTIMIZING (P1) WITH A MINI-BATCH STOCHASTIC GRADIENT METHOD

The training loss at each mini-batch is

$$\begin{aligned}\mathcal{L} &= \frac{1}{B} \sum_{r=1}^{2R} \sum_{b=1}^B \left(X_{rb} - \mathbf{D}_r \mathcal{T}_{\exp(\alpha)} \left(\mathbf{E} \mathbf{X}_b^{(i-1)} \right) \right)^2 \\ &= \sum_{r=1}^{2R} \sum_{b=1}^B \frac{1}{B} \left[X_{rb} - \mathbf{D}_r \left(\sum_{r=1}^{2R} \mathbf{E}_r X_{rb}^{(i-1)} - \exp(\alpha) \odot \right. \right. \\ &\quad \left. \left. \text{sign} \left(\sum_{r=1}^{2R} \mathbf{E}_r X_{rb}^{(i-1)} \right) \right) \odot \mathbb{1}_{|\mathbf{E} \mathbf{X}_b^{(i-1)}| > \exp(\alpha)} \right]^2,\end{aligned}$$

where \mathbf{D}_r is the r th row of \mathbf{D} , \mathbf{E}_r is the r th column of \mathbf{E} , $(\cdot)_{rb}$ denotes the element at r th row and b th column of the matrix. Therefore, subgradient of (P1) with respect to α at each mini-batch is

$$\begin{aligned}\frac{\partial \mathcal{L}(\mathbf{D}, \mathbf{E}, \alpha)}{\partial \alpha} &= \frac{2}{B} \sum_{r=1}^{2R} \sum_{b=1}^B \left[X_{rb} - \mathbf{D}_r \mathcal{T}_{\exp(\alpha)} \left(\mathbf{E} \mathbf{X}_b^{(i-1)} \right) \right] \cdot \frac{\partial \mathbf{D}_r \left[\exp(\alpha) \odot \text{sign} \left(\sum_{r=1}^{2R} \mathbf{E}_r X_{rb}^{(i-1)} \right) \right] \odot \mathbb{1}_{|\mathbf{E} \mathbf{X}_b^{(i-1)}| > \exp(\alpha)}}{\partial \alpha} \\ &= \frac{2}{B} \sum_{r=1}^{2R} \sum_{b=1}^B \left[X_{rb} - \mathbf{D}_r \mathcal{T}_{\exp(\alpha)} \left(\mathbf{E} \mathbf{X}_b^{(i-1)} \right) \right] \cdot \mathbf{D}_r^\top \odot \\ &\quad \exp(\alpha) \odot \text{sign} \left(\mathbf{E} \mathbf{X}_b^{(i-1)} \right) \odot \mathbb{1}_{|\mathbf{E} \mathbf{X}_b^{(i-1)}| > \exp(\alpha)} \\ &= \frac{2}{B} \left\{ \mathbf{D}^\top \left(\mathbf{X} - \mathbf{D} \mathbf{Z}^{(i-1)} \right) \odot \exp(\alpha \mathbf{1}') \odot \text{sign} \left(\mathbf{E} \mathbf{X}^{(i-1)} \right) \odot \right. \\ &\quad \left. \mathbb{1}_{|\mathbf{E} \mathbf{X}^{(i-1)}| > \exp(\alpha \mathbf{1}')} \right\} \mathbf{1} \\ &= \frac{2}{B} \left\{ \mathbf{D}^\top \left(\mathbf{X} - \mathbf{D} \mathbf{Z}^{(i-1)} \right) \odot \exp(\alpha \mathbf{1}') \odot \text{sign} \left(\mathbf{Z}^{(i-1)} \right) \right\} \mathbf{1}.\end{aligned}$$

We can easily obtain subgradient of \mathcal{L} with respect to \mathbf{D} at each mini-batch as

$$\frac{\partial \mathcal{L}}{\partial \mathbf{D}} = -\frac{2}{B} \left(\mathbf{X} - \mathbf{D} \mathbf{Z}^{(i-1)} \right) \cdot \mathbf{Z}^{(i-1)\top}.$$

At each mini-batch, the subgradient of \mathcal{L} with respect to r_1 th column of \mathbf{E} is as follows:

$$\begin{aligned}\frac{\partial \mathcal{L}(\mathbf{D}, \mathbf{E}, \alpha)}{\partial \mathbf{E}_{r_1}} &= -\frac{2}{B} \sum_{r=1}^{2R} \sum_{b=1}^B \left(X_{rb} - \mathbf{D}_r \mathcal{T}_{\exp(\alpha)} \left(\mathbf{E} \mathbf{X}_b^{(i-1)} \right) \right) \cdot \\ &\quad \mathbf{D}_r^\top \odot \mathbb{1}_{|\mathbf{E} \mathbf{X}_b^{(i-1)}| > \exp(\alpha)} \cdot X_{r_1 b}^{(i-1)} \\ &= -\frac{2}{B} \sum_{b=1}^B \mathbf{D}^\top \left(\mathbf{X}_b - \mathbf{D} \mathcal{T}_{\exp(\alpha)} \left(\mathbf{E} \mathbf{X}_b^{(i-1)} \right) \right) \odot \\ &\quad \mathbb{1}_{|\mathbf{E} \mathbf{X}_b^{(i-1)}| > \exp(\alpha)} \cdot X_{r_1 b}^{(i-1)} \\ &= -\frac{2}{B} \mathbf{D}^\top \left(\mathbf{X} - \mathbf{D} \mathbf{Z}^{(i-1)} \right) \odot \mathbb{1}_{|\mathbf{E} \mathbf{X}^{(i-1)}| > \exp(\alpha \mathbf{1}')} \cdot \mathbf{X}_{r_1}^{(i-1)\top}.\end{aligned}$$

Thus, the subgradient of \mathcal{L} with respect to \mathbf{E} for each mini-batch selection is

$$\frac{\partial \mathcal{L}(\mathbf{D}, \mathbf{E}, \alpha)}{\partial \mathbf{E}} = -\frac{2}{B} \mathbf{D}^\top \left(\mathbf{X} - \mathbf{D} \mathcal{T}_{\exp(\alpha \mathbf{1}')} \left(\mathbf{E} \mathbf{X}^{(i-1)} \right) \right) \odot \mathbb{1}_{|\mathbf{E} \mathbf{X}^{(i-1)}| > \exp(\alpha \mathbf{1}')} \cdot \mathbf{X}^{(i-1)\top}$$

S.II. TRAINING INDIVIDUAL-MATERIAL BCD-NETS IN SECTION. III-C

At the i th iteration, the training loss of distinct individual-material BCD-Nets for m th material is

$$\mathcal{L}(\mathbf{D}_{m,m}, \mathbf{E}_{m,m}, \alpha_m) := \frac{1}{P} \|\tilde{\mathbf{X}}_m - \mathbf{D}_{m,m} \mathcal{T}_{\exp(\alpha_m)}(\mathbf{E}_{m,m} \tilde{\mathbf{X}}_m^{(i-1)})\|_{\mathbb{F}}^2.$$

The subgradient of $\mathcal{L}(\mathbf{D}_{m,m}, \mathbf{E}_{m,m}, \alpha_m)$ with respect to $\mathbf{D}_{m,m}$, $\mathbf{E}_{m,m}$, and α_m for each mini-batch selection are as follows:

$$\begin{aligned}\frac{\partial \mathcal{L}(\mathbf{D}_{m,m}, \mathbf{E}_{m,m}, \alpha_m)}{\partial \mathbf{D}_{m,m}} &= -\frac{2}{B} \left(\mathbf{X}_m - \mathbf{D}_{m,m} \mathbf{Z}_m^{(i-1)} \right) \mathbf{Z}_m^{(i-1)\top} \\ \frac{\partial \mathcal{L}(\mathbf{D}_{m,m}, \mathbf{E}_{m,m}, \alpha_m)}{\partial \mathbf{E}_{m,m}} &= -\frac{2}{B} \mathbf{D}_{m,m}^\top \left(\mathbf{X}_m - \mathbf{D}_{m,m} \mathbf{Z}_m^{(i-1)} \right) \\ &\quad \odot \mathbb{1}_{|\mathbf{E}_{m,m} \mathbf{X}_m^{(i-1)}| > \exp(\alpha_m \mathbf{1}')} \cdot \mathbf{X}_m^{(i-1)\top} \\ \frac{\partial \mathcal{L}(\mathbf{D}_{m,m}, \mathbf{E}_{m,m}, \alpha_m)}{\partial \alpha_m} &= \frac{2}{B} \left\{ \mathbf{D}_{m,m}^\top \left(\mathbf{X}_m - \mathbf{D}_{m,m} \mathbf{Z}_m^{(i-1)} \right) \odot \exp(\alpha_m \mathbf{1}') \odot \text{sign} \left(\mathbf{Z}_m^{(i-1)} \right) \right\} \mathbf{1},\end{aligned}$$

where $\mathbf{X}_m, \mathbf{X}_m^{(i-1)} \in \mathbb{R}^{R \times B}$ are mini-batch in which columns are randomly selected from $\tilde{\mathbf{X}}_m$ and $\tilde{\mathbf{X}}_m^{(i-1)}$, respectively, and $\mathbf{Z}_m^{(i-1)} = \mathcal{T}_{\exp(\alpha_m \mathbf{1}')}(\mathbf{E}_{m,m} \mathbf{X}_m^{(i-1)})$.

S.III. RELATION BETWEEN CONVOLUTION-PERSPECTIVE AND PATCH-BASED TRAININGS OF DISTINCT CROSS-MATERIAL MODEL

Proposition S.1. *The distinct cross-material CNN refiner in (1) can be rewritten with patch-based perspective as follows (we omit the iteration superscript indices (i) for simplicity):*

$$\begin{bmatrix} \sum_{k=1}^K \sum_{n=1}^2 \mathbf{d}_{1,n,k} * \mathcal{T}_{\exp(\alpha_{n,k})} \left(\sum_{m=1}^2 \mathbf{e}_{n,m,k} * \mathbf{x}_m \right) \\ \sum_{k=1}^K \sum_{n=1}^2 \mathbf{d}_{2,n,k} * \mathcal{T}_{\exp(\alpha_{n,k})} \left(\sum_{m=1}^2 \mathbf{e}_{n,m,k} * \mathbf{x}_m \right) \end{bmatrix} = \frac{1}{R} \sum_{j=1}^N \bar{\mathbf{P}}_j^\top \mathbf{D} \mathcal{T}_{\exp(\alpha)} (\mathbf{E} \bar{\mathbf{P}}_j \mathbf{x}), \quad (\text{S.1})$$

where $\mathbf{x} = [\mathbf{x}_1^\top, \mathbf{x}_2^\top]^\top$. See other related notations in (1) and (8).

Proof. First, we have the following reformulation [2, S.1]:

$$\begin{bmatrix} \mathbf{e}_{n,m,1} * \mathbf{u} \\ \vdots \\ \mathbf{e}_{n,m,K} * \mathbf{u} \end{bmatrix} = \mathbf{P} \begin{bmatrix} \mathbf{E}_{n,m} \mathbf{P}_1 \\ \vdots \\ \mathbf{E}_{n,m} \mathbf{P}_N \end{bmatrix} \mathbf{u} := \tilde{\mathbf{E}}_{n,m} \mathbf{u},$$

where $\mathbf{P} \in \mathbb{R}^{KN \times KN}$ is a permutation matrix. Considering that

$$\sum_{k=1}^K \bar{\mathbf{e}}_{n,m,k} * (\mathbf{e}_{n,m,k} * \mathbf{u}) = \frac{1}{R} \tilde{\mathbf{E}}_{n,m}^H \tilde{\mathbf{E}}_{n,m} \mathbf{u},$$

we have

$$\sum_{k=1}^K \mathbf{d}_{1,1,k} * (\mathbf{e}_{1,1,k} * \mathbf{x}_1) = \frac{1}{R} \tilde{\mathbf{D}}_{1,1} \tilde{\mathbf{E}}_{1,1} \mathbf{x}_1 \quad \text{and} \quad \sum_{k=1}^K \mathbf{d}_{1,1,k} * (\mathbf{e}_{1,2,k} * \mathbf{x}_2) = \frac{1}{R} \tilde{\mathbf{D}}_{1,1} \tilde{\mathbf{E}}_{1,2} \mathbf{x}_2.$$

Then we obtain the following reformulation result for term $\sum_{k=1}^K \mathbf{d}_{1,1,k} * \mathcal{T}_{\exp(\alpha_{1,k})} (\mathbf{e}_{1,1,k} * \mathbf{x}_1 + \mathbf{e}_{1,2,k} * \mathbf{x}_2)$:

$$\sum_{k=1}^K \mathbf{d}_{1,1,k} * \mathcal{T}_{\exp(\alpha_{1,k})} (\mathbf{e}_{1,1,k} * \mathbf{x}_1 + \mathbf{e}_{1,2,k} * \mathbf{x}_2) = \frac{1}{R} \sum_{j=1}^N \mathbf{P}_j^\top \mathbf{D}_{1,1} \mathcal{T}_{\exp(\alpha_1)} (\mathbf{E}_{1,1} \mathbf{P}_j \mathbf{x}_1 + \mathbf{E}_{1,2} \mathbf{P}_j \mathbf{x}_2), \quad (\text{S.2})$$

where we use the permutation invariance of thresholding operator [3, S.8] and $\mathbf{P}^\top \mathbf{P} = \mathbf{I}$. Similarly, for term $\sum_{k=1}^K \mathbf{d}_{1,2,k} * \mathcal{T}_{\exp(\alpha_{2,k})} (\mathbf{e}_{2,1,k} * \mathbf{x}_1 + \mathbf{e}_{2,2,k} * \mathbf{x}_2)$, we have

$$\sum_{k=1}^K \mathbf{d}_{1,2,k} * \mathcal{T}_{\exp(\alpha_{2,k})} (\mathbf{e}_{2,1,k} * \mathbf{x}_1 + \mathbf{e}_{2,2,k} * \mathbf{x}_2) = \frac{1}{R} \sum_{j=1}^N \mathbf{P}_j^\top \mathbf{D}_{1,2} \mathcal{T}_{\exp(\alpha_2)} (\mathbf{E}_{2,1} \mathbf{P}_j \mathbf{x}_1 + \mathbf{E}_{2,2} \mathbf{P}_j \mathbf{x}_2). \quad (\text{S.3})$$

Combining (S.2) and (S.3) gives the following result:

$$\begin{aligned} \sum_{k=1}^K \sum_{n=1}^2 \mathbf{d}_{1,n,k} * \mathcal{T}_{\exp(\alpha_{n,k})} \left(\sum_{m=1}^2 \mathbf{e}_{n,m,k} * \mathbf{x}_m \right) &= \frac{1}{R} \sum_{j=1}^N \mathbf{P}_j^\top \mathbf{D}_{1,1} \mathcal{T}_{\exp(\alpha_1)} (\mathbf{E}_{1,1} \mathbf{P}_j \mathbf{x}_1 + \mathbf{E}_{1,2} \mathbf{P}_j \mathbf{x}_2) + \\ &\quad \frac{1}{R} \sum_{j=1}^N \mathbf{P}_j^\top \mathbf{D}_{1,2} \mathcal{T}_{\exp(\alpha_2)} (\mathbf{E}_{2,1} \mathbf{P}_j \mathbf{x}_1 + \mathbf{E}_{2,2} \mathbf{P}_j \mathbf{x}_2). \end{aligned} \quad (\text{S.4})$$

Similar to (S.4), we have

$$\begin{aligned} \sum_{k=1}^K \sum_{n=1}^2 \mathbf{d}_{2,n,k} * \mathcal{T}_{\exp(\alpha_{n,k})} \left(\sum_{m=1}^2 \mathbf{e}_{n,m,k} * \mathbf{x}_m \right) &= \frac{1}{R} \sum_{j=1}^N \mathbf{P}_j^\top \mathbf{D}_{2,1} \mathcal{T}_{\exp(\alpha_1)} (\mathbf{E}_{1,1} \mathbf{P}_j \mathbf{x}_1 + \mathbf{E}_{1,2} \mathbf{P}_j \mathbf{x}_2) + \\ &\quad \frac{1}{R} \sum_{j=1}^N \mathbf{P}_j^\top \mathbf{D}_{2,2} \mathcal{T}_{\exp(\alpha_2)} (\mathbf{E}_{2,1} \mathbf{P}_j \mathbf{x}_1 + \mathbf{E}_{2,2} \mathbf{P}_j \mathbf{x}_2). \end{aligned} \quad (\text{S.5})$$

Combining the results in (S.4) and (S.5) completes the proof.

Proposition S.2. *The loss function for training the distinct cross-material CNN refiner in (1) is bounded by its patch-based training loss function:*

$$\frac{1}{2L} \sum_{l=1}^L \left\| \begin{bmatrix} \mathbf{x}_{l,1} \\ \mathbf{x}_{l,2} \end{bmatrix} - \begin{bmatrix} \sum_{k=1}^K \sum_{n=1}^2 \mathbf{d}_{1,n,k} * \mathcal{T}_{\exp(\alpha_{n,k})} \left(\sum_{m=1}^2 \mathbf{e}_{n,m,k} * \mathbf{x}_{l,m}^{(i-1)} \right) \\ \sum_{k=1}^K \sum_{n=1}^2 \mathbf{d}_{2,n,k} * \mathcal{T}_{\exp(\alpha_{n,k})} \left(\sum_{m=1}^2 \mathbf{e}_{n,m,k} * \mathbf{x}_{l,m}^{(i-1)} \right) \end{bmatrix} \right\|_2^2 \leq \frac{1}{2LR} \sum_{l=1}^L \left\| \begin{bmatrix} \tilde{\mathbf{X}}_{l,1} \\ \tilde{\mathbf{X}}_{l,2} \end{bmatrix} - \mathbf{D} \mathcal{T}_{\exp(\alpha)} \left(\mathbf{E} \begin{bmatrix} \tilde{\mathbf{X}}_{l,1}^{(i-1)} \\ \tilde{\mathbf{X}}_{l,2}^{(i-1)} \end{bmatrix} \right) \right\|_F^2, \quad (\text{S.6})$$

where $\mathbf{x}_{l,m}$ and $\mathbf{x}_{l,m}^{(i-1)}$ are the l th high-quality and degraded images of the m th material, respectively, for $l = 1, \dots, L$ and $m = 1, 2$, $\tilde{\mathbf{X}}_{l,m} \in \mathbb{R}^{R \times N}$ and $\tilde{\mathbf{X}}_{l,m}^{(i-1)} \in \mathbb{R}^{R \times N}$ are matrices whose columns are vectorized patches extracted from images $\mathbf{x}_{l,m}$ and $\mathbf{x}_{l,m}^{(i-1)}$ (with a spatial patch stride of 1×1), respectively. See related notations in (1), (8), and Section. III-A.

Proof. Based on Proposition S.1, we obtain the result as follows:

$$\begin{aligned} & \frac{1}{2L} \sum_{l=1}^L \left\| \begin{bmatrix} \mathbf{x}_{l,1} \\ \mathbf{x}_{l,2} \end{bmatrix} - \begin{bmatrix} \sum_{k=1}^K \sum_{n=1}^2 \mathbf{d}_{1,n,k} * \mathcal{T}_{\exp(\alpha_{n,k})} \left(\sum_{m=1}^2 \mathbf{e}_{n,m,k} * \mathbf{x}_{l,m}^{(i-1)} \right) \\ \sum_{k=1}^K \sum_{n=1}^2 \mathbf{d}_{2,n,k} * \mathcal{T}_{\exp(\alpha_{n,k})} \left(\sum_{m=1}^2 \mathbf{e}_{n,m,k} * \mathbf{x}_{l,m}^{(i-1)} \right) \end{bmatrix} \right\|_2^2 \\ &= \frac{1}{2L} \sum_{l=1}^L \left\| \begin{bmatrix} \mathbf{x}_{l,1} \\ \mathbf{x}_{l,2} \end{bmatrix} - \frac{1}{R} \begin{bmatrix} \sum_{j=1}^N \mathbf{P}_j^\top \mathbf{D}_{1,1} \mathcal{T}_{\exp(\alpha_1)} \left(\mathbf{E}_{1,1} \mathbf{P}_j \mathbf{x}_{l,1}^{(i-1)} + \mathbf{E}_{1,2} \mathbf{P}_j \mathbf{x}_{l,2}^{(i-1)} \right) + \sum_{j=1}^N \mathbf{P}_j^\top \mathbf{D}_{1,2} \mathcal{T}_{\exp(\alpha_2)} \left(\mathbf{E}_{2,1} \mathbf{P}_j \mathbf{x}_{l,1}^{(i-1)} + \mathbf{E}_{2,2} \mathbf{P}_j \mathbf{x}_{l,2}^{(i-1)} \right) \\ \sum_{j=1}^N \mathbf{P}_j^\top \mathbf{D}_{2,1} \mathcal{T}_{\exp(\alpha_1)} \left(\mathbf{E}_{1,1} \mathbf{P}_j \mathbf{x}_{l,1}^{(i-1)} + \mathbf{E}_{1,2} \mathbf{P}_j \mathbf{x}_{l,2}^{(i-1)} \right) + \sum_{j=1}^N \mathbf{P}_j^\top \mathbf{D}_{2,2} \mathcal{T}_{\exp(\alpha_2)} \left(\mathbf{E}_{2,1} \mathbf{P}_j \mathbf{x}_{l,1}^{(i-1)} + \mathbf{E}_{2,2} \mathbf{P}_j \mathbf{x}_{l,2}^{(i-1)} \right) \end{bmatrix} \right\|_2^2 \\ &= \frac{1}{2LR^2} \sum_{l=1}^L \left\| \begin{bmatrix} \sum_{j=1}^N \mathbf{P}_j^\top \mathbf{P}_j \mathbf{x}_{l,1} \\ \sum_{j=1}^N \mathbf{P}_j^\top \mathbf{P}_j \mathbf{x}_{l,2} \end{bmatrix} - \begin{bmatrix} \sum_{j=1}^N \mathbf{P}_j^\top \left(\mathbf{D}_{1,1} \mathcal{T}_{\exp(\alpha_1)} \left(\mathbf{E}_{1,1} \mathbf{P}_j \mathbf{x}_{l,1}^{(i-1)} + \mathbf{E}_{1,2} \mathbf{P}_j \mathbf{x}_{l,2}^{(i-1)} \right) + \mathbf{D}_{1,2} \mathcal{T}_{\exp(\alpha_2)} \left(\mathbf{E}_{2,1} \mathbf{P}_j \mathbf{x}_{l,1}^{(i-1)} + \mathbf{E}_{2,2} \mathbf{P}_j \mathbf{x}_{l,2}^{(i-1)} \right) \right) \\ \sum_{j=1}^N \mathbf{P}_j^\top \left(\mathbf{D}_{2,1} \mathcal{T}_{\exp(\alpha_1)} \left(\mathbf{E}_{1,1} \mathbf{P}_j \mathbf{x}_{l,1}^{(i-1)} + \mathbf{E}_{1,2} \mathbf{P}_j \mathbf{x}_{l,2}^{(i-1)} \right) + \mathbf{D}_{2,2} \mathcal{T}_{\exp(\alpha_2)} \left(\mathbf{E}_{2,1} \mathbf{P}_j \mathbf{x}_{l,1}^{(i-1)} + \mathbf{E}_{2,2} \mathbf{P}_j \mathbf{x}_{l,2}^{(i-1)} \right) \right) \end{bmatrix} \right\|_2^2 \\ &\leq \frac{1}{2LR} \sum_{l=1}^L \sum_{j=1}^N \left\| \begin{bmatrix} \tilde{\mathbf{X}}_{l,1,j} \\ \tilde{\mathbf{X}}_{l,2,j} \end{bmatrix} - \begin{bmatrix} \mathbf{D}_{1,1} & \mathbf{D}_{1,2} \\ \mathbf{D}_{2,1} & \mathbf{D}_{2,2} \end{bmatrix} \mathcal{T}_{\exp(\alpha)} \left(\begin{bmatrix} \mathbf{E}_{1,1} & \mathbf{E}_{1,2} \\ \mathbf{E}_{2,1} & \mathbf{E}_{2,2} \end{bmatrix} \begin{bmatrix} \tilde{\mathbf{X}}_{l,1,j}^{(i-1)} \\ \tilde{\mathbf{X}}_{l,2,j}^{(i-1)} \end{bmatrix} \right) \right\|_2^2 \\ &= \frac{1}{2LR} \sum_{l=1}^L \left\| \begin{bmatrix} \tilde{\mathbf{X}}_{l,1} \\ \tilde{\mathbf{X}}_{l,2} \end{bmatrix} - \mathbf{D} \mathcal{T}_{\exp(\alpha)} \left(\mathbf{E} \begin{bmatrix} \tilde{\mathbf{X}}_{l,1}^{(i-1)} \\ \tilde{\mathbf{X}}_{l,2}^{(i-1)} \end{bmatrix} \right) \right\|_F^2, \end{aligned}$$

where $\tilde{\mathbf{X}}_{l,m,j}^{(i-1)} \in \mathbb{R}^R$ and $\tilde{\mathbf{X}}_{l,m,j} \in \mathbb{R}^R$ are the j th column of $\tilde{\mathbf{X}}_{l,m}^{(i-1)}$ and $\tilde{\mathbf{X}}_{l,m}$, respectively. Here, the inequality holds by $\tilde{\mathbf{P}} \tilde{\mathbf{P}}^\top \preceq R \cdot \mathbf{I}$ with $\tilde{\mathbf{P}} := [\mathbf{P}_1^\top, \dots, \mathbf{P}_N^\top]^\top$.

S.IV. ADDITIONAL RESULTS

Fig. S.1 shows the #3 material density images decomposed by four BCD-Net methods. Distinct cross-material BCD-Net significantly reduces artifacts at the boundaries of water and bone compared to other three BCD-Net methods.

Fig. S.2 and Fig. S.3 show another two test slices comparisons. DCNN improves decomposition quality compared to DECT-EP and DECT-ST in terms of reducing noise and artifacts, but it still retains some streak artifacts. Compared to DCNN, distinct cross-material BCD-Net further removes noise and artifacts, and improves the sharpness of edges in soft tissue.

Fig. S.4 shows the convergence of RMSE of water and bone images for four BCD-Net methods over iterations. Distinct cross-material BCD-Net achieves the lowest RMSE and shows quick convergence.

Fig. S.5 shows decomposed material density images by four BCD-Net methods for clinical head data. Distinct cross-material BCD-Net removes noise and artifacts, e.g., the left-most zoom-ins in water images, and recovers details more precisely, e.g., structures inside red circles numbered 1 and 2.

REFERENCES

- [1] Z. Li, Y. Long, and I. Y. Chun, "An improved iterative neural network for high-quality image-domain material decomposition in dual-energy CT," submitted, Nov. 2020.
- [2] I. Y. Chun and J. A. Fessler, "Convolutional analysis operator learning: Acceleration and convergence," *IEEE Trans. Im. Proc.*, vol. 29, pp. 2108–2122, 2020.
- [3] I. Y. Chun, Z. Huang, H. Lim, and J. A. Fessler, "Momentum-Net: Fast and convergent iterative neural network for inverse problems," early access in *IEEE Trans. Pattern Anal. Mach. Intell.*, Jul. 2020, DOI: 10.1109/TPAMI.2020.3012955.

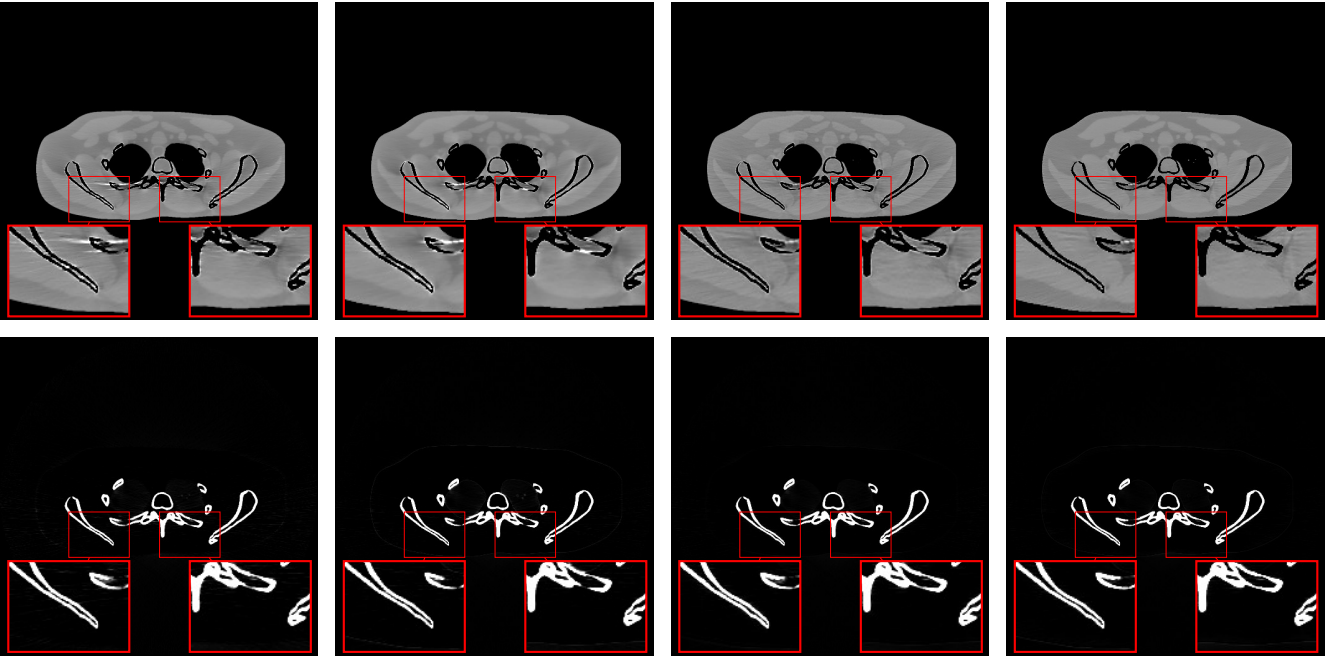


Fig. S.1: Left to right: material density images of #3 decomposed by identical individual-material BCD-Net, identical cross-material BCD-Net, distinct individual-material BCD-Net, and distinct cross-material BCD-Net. The top and bottom rows show the water and bone images with display windows $[0.7 \ 1.3] \text{ g/cm}^3$ and $[0 \ 0.8] \text{ g/cm}^3$, respectively.

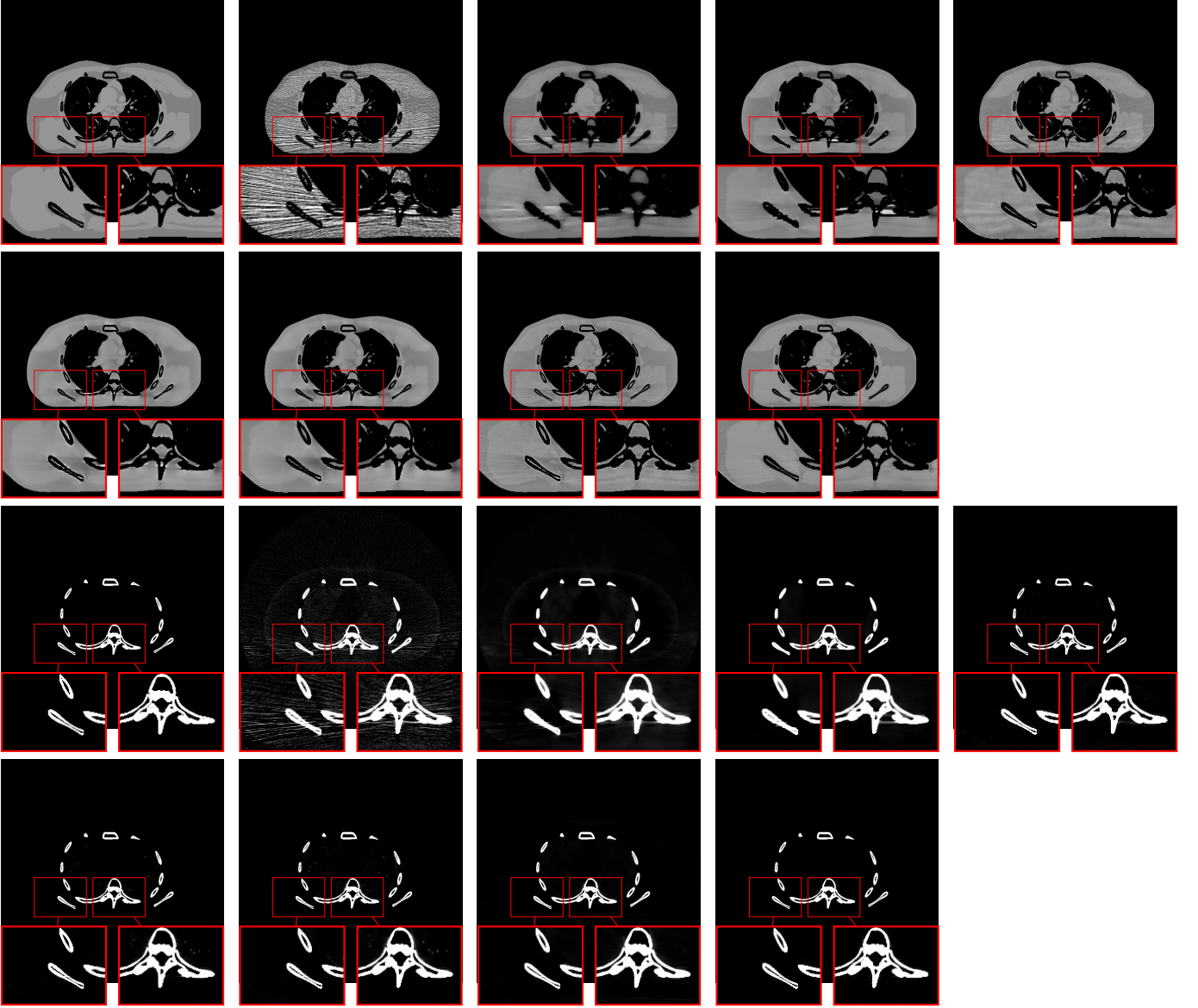


Fig. S.2: Decompositions of #1 of XCAT phantom. First and third rows are water and bone images of ground truth, direct matrix inversion, DECT-EP, DECT-ST, and DCNN. Second and fourth rows are water and bone images of identical individual-material BCD-Net, identical cross-material BCD-Net, distinct individual-material BCD-Net, and distinct cross-material BCD-Net. Water and bone images are shown with display windows $[0.7 \ 1.3] \text{ g/cm}^3$ and $[0 \ 0.8] \text{ g/cm}^3$, respectively.

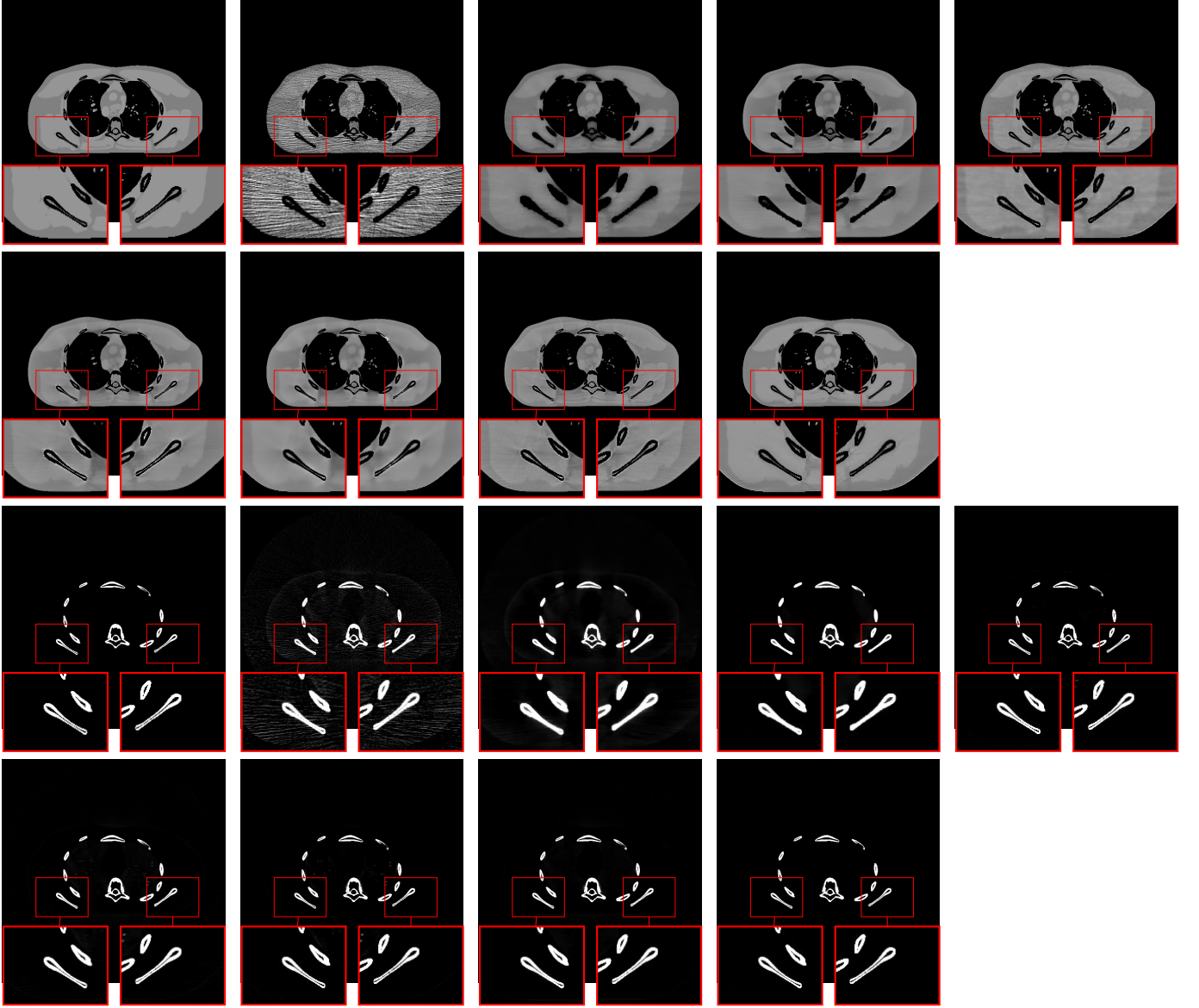


Fig. S.3: Decompositions of #2 of XCAT phantom. First and third rows are water and bone images of ground truth, direct matrix inversion, DECT-EP, DECT-ST, and DCNN. Second and fourth rows are water and bone images of identical individual-material BCD-Net, identical cross-material BCD-Net, distinct individual-material BCD-Net, and distinct cross-material BCD-Net. Water and bone images are shown with display windows $[0.7 \ 1.3] \text{ g/cm}^3$ and $[0 \ 0.8] \text{ g/cm}^3$, respectively.

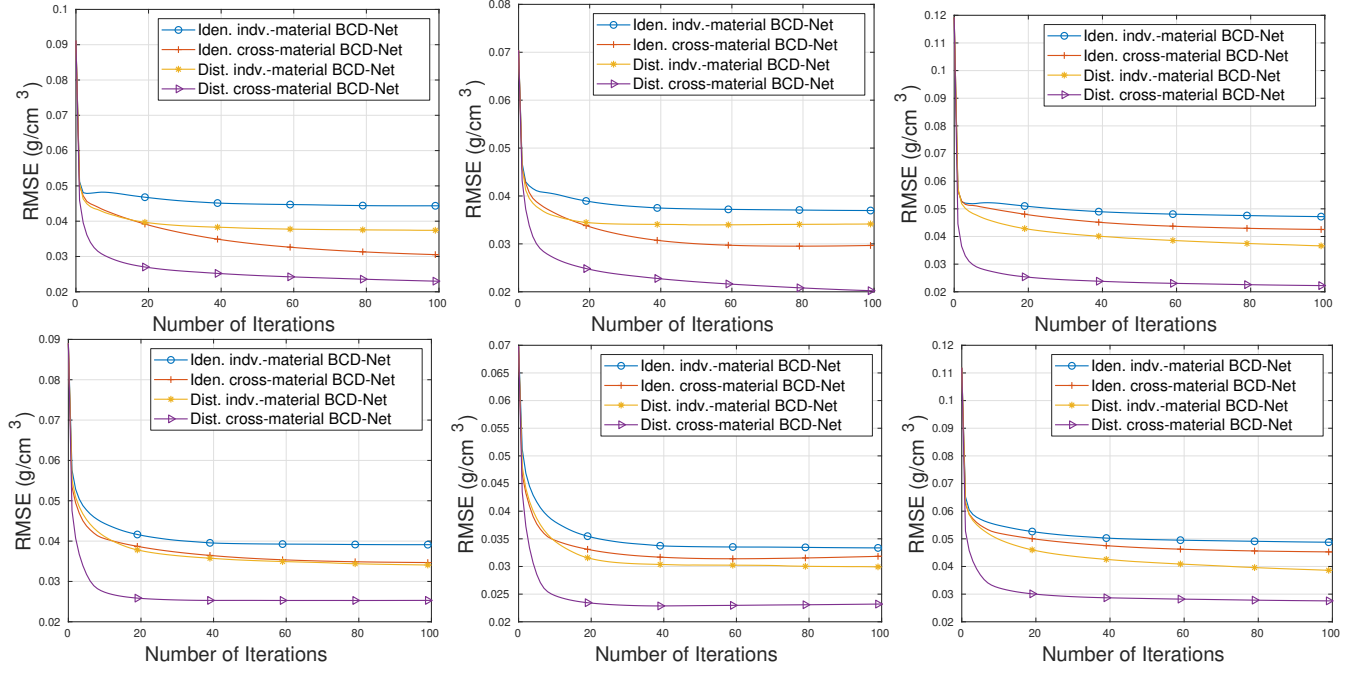


Fig. S.4: RMSE for three different test slices of XCAT phantom plotted over iterations of four BCD-Net methods. From left to right: RMSE for Test #1, Test #2, and Test #3 of the XCAT phantom. Top and bottom rows correspond to the RMSE of water and bone images, respectively.

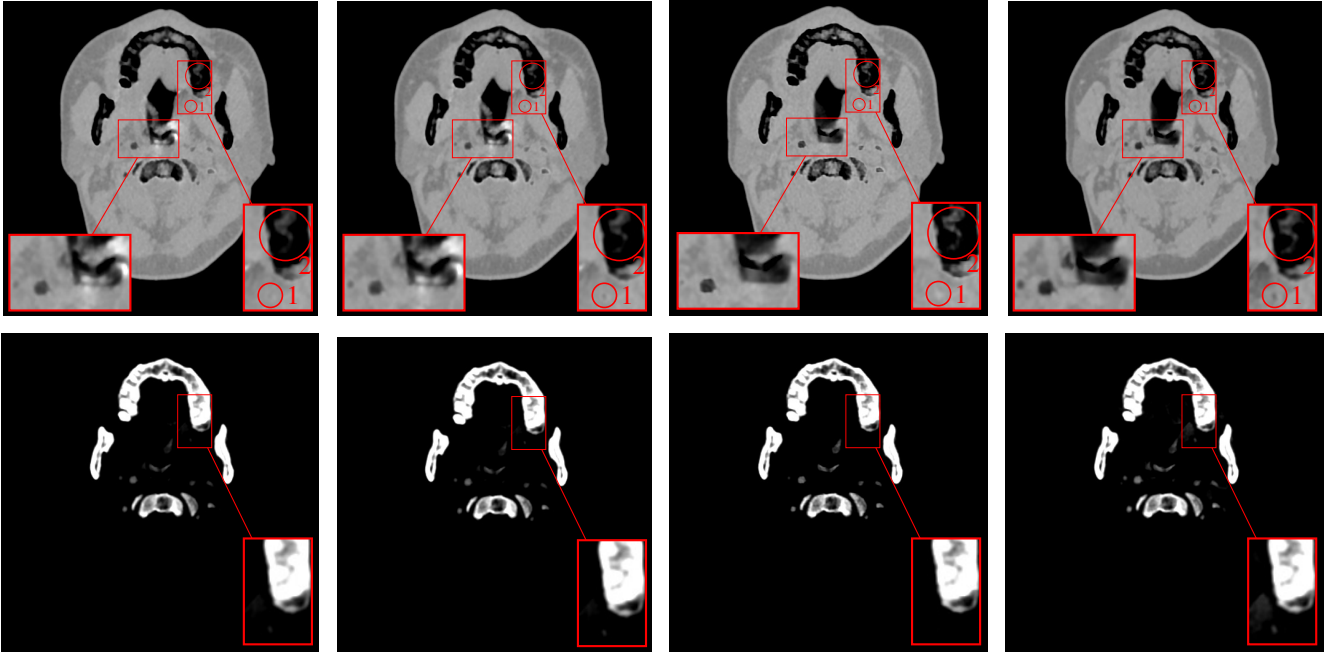


Fig. S.5: Left to right: material images decomposed by identical individual-material BCD-Net, identical cross-material BCD-Net, distinct individual-material BCD-Net, and distinct cross-material BCD-Net. The top and bottom rows show the water and bone images with display windows $[0.5 \ 1.3] \text{ g/cm}^3$ and $[0.05 \ 0.905] \text{ g/cm}^3$, respectively.